



NAVAL POSTGRADUATE SCHOOL

MONTEREY, CALIFORNIA

THESIS

**3-D ACOUSTIC SCATTERING FROM 2-D ROUGH
SURFACES USING A PARABOLIC EQUATION MODEL**

by

Ahmed M. Helmy

December 2013

Thesis Advisor:
Second Reader:

Kevin B. Smith
Daphne Kapolka

Approved for public release; distribution is unlimited

THIS PAGE INTENTIONALLY LEFT BLANK

REPORT DOCUMENTATION PAGE			<i>Form Approved OMB No. 0704-0188</i>	
Public reporting burden for this collection of information is estimated to average 1 hour per response, including the time for reviewing instruction, searching existing data sources, gathering and maintaining the data needed, and completing and reviewing the collection of information. Send comments regarding this burden estimate or any other aspect of this collection of information, including suggestions for reducing this burden, to Washington headquarters Services, Directorate for Information Operations and Reports, 1215 Jefferson Davis Highway, Suite 1204, Arlington, VA 22202-4302, and to the Office of Management and Budget, Paperwork Reduction Project (0704-0188) Washington, DC 20503.				
1. AGENCY USE ONLY (Leave blank)		2. REPORT DATE December 2013	3. REPORT TYPE AND DATES COVERED Master's Thesis	
4. TITLE AND SUBTITLE 3-D ACOUSTIC SCATTERING FROM 2-D ROUGH SURFACES USING A PARABOLIC EQUATION MODEL			5. FUNDING NUMBERS	
6. AUTHOR(S) Ahmed M. Helmy				
7. PERFORMING ORGANIZATION NAME(S) AND ADDRESS(ES) Naval Postgraduate School Monterey, CA 93943-5000			8. PERFORMING ORGANIZATION REPORT NUMBER	
9. SPONSORING /MONITORING AGENCY NAME(S) AND ADDRESS(ES) N/A			10. SPONSORING/MONITORING AGENCY REPORT NUMBER	
11. SUPPLEMENTARY NOTES The views expressed in this thesis are those of the author and do not reflect the official policy or position of the Department of Defense or the U.S. Government. IRB Protocol number ____N/A____.				
12a. DISTRIBUTION / AVAILABILITY STATEMENT Approved for public release; distribution is unlimited			12b. DISTRIBUTION CODE	
13. ABSTRACT (maximum 200 words) Rough surface scattering plays a crucial role in the statistics of acoustic propagation signals, especially at mid-frequencies and higher (e.g., acoustic communications systems). For many years, the effects of rough surface scattering were computed using simple models that were applied in two dimensions (2-D) only. A prescribed method of computing 2-D rough surface scattering directly in a parabolic equation model based on the Split-Step Fourier algorithm was introduced by Tappert and Nghiem-Phu in the mid-1980s. This method has been successfully implemented in various 2-D parabolic equation models, including the Monterey Miami Parabolic Equation model. However, some scientific research of more formal scattering predictions have suggested that out-of-plane, three dimensional (3-D) scattering may lead to significant disparities in the scattered field statistics. Introducing a hybrid implementation for the scattering effect in the field transformation equations using a tri-diagonal solution with the Padé approximant to obtain a system of equations for azimuthal corrections will support predictions of the effect of surface scattering on 3-D propagation, which is critical in evaluating the variability in underwater acoustic propagation. Results of the 3-D scattering calculations obtained are compared with the output of basic 2-D interface perturbations utilizing the standard 2-D approach.				
14. SUBJECT TERMS Acoustic Propagation, Acoustic Scattering, Sea Surface Perturbations, Split-Step Fourier Algorithm, Finite Difference Algorithm.			15. NUMBER OF PAGES 73	
			16. PRICE CODE	
17. SECURITY CLASSIFICATION OF REPORT Unclassified	18. SECURITY CLASSIFICATION OF THIS PAGE Unclassified	19. SECURITY CLASSIFICATION OF ABSTRACT Unclassified	20. LIMITATION OF ABSTRACT UU	

THIS PAGE INTENTIONALLY LEFT BLANK

Approved for public release; distribution is unlimited

**3-D ACOUSTIC SCATTERING FROM 2-D ROUGH SURFACES USING A
PARABOLIC EQUATION MODEL**

Ahmed M. Helmy
Lieutenant, Egyptian Naval Forces
B.S, Egyptian Naval Academy, 2004
MSc, Arab Academy for Science and Technology, 2012

Submitted in partial fulfillment of the
requirements for the degree of

MASTER OF SCIENCE IN ENGINEERING ACOUSTICS

from the

**NAVAL POSTGRADUATE SCHOOL
December 2013**

Author: Ahmed M. Helmy

Approved by: Kevin B. Smith
Thesis Advisor

Daphne Kapolka
Second Reader

Daphne Kapolka
Chair, Engineering Acoustics Academic Committee

THIS PAGE INTENTIONALLY LEFT BLANK

ABSTRACT

Rough surface scattering plays a crucial role in the statistics of acoustic propagation signals, especially at mid-frequencies and higher (e.g., acoustic communications systems). For many years, the effects of rough surface scattering were computed using simple models that were applied in two dimensions (2-D) only.

A prescribed method of computing 2-D rough surface scattering directly in a parabolic equation model based on the Split-Step Fourier algorithm was introduced by Tappert and Nghiem-Phu in the mid-1980s. This method has been successfully implemented in various 2-D parabolic equation models, including the Monterey Miami Parabolic Equation model. However, some scientific research of more formal scattering predictions have suggested that out-of-plane, three dimensional (3-D) scattering may lead to significant disparities in the scattered field statistics. Introducing a hybrid implementation for the scattering effect in the field transformation equations using a tri-diagonal solution with the Padé approximant to obtain a system of equations for azimuthal corrections will support predictions of the effect of surface scattering on 3-D propagation, which is critical in evaluating the variability in underwater acoustic propagation. Results of the 3-D scattering calculations obtained are compared with the output of basic 2-D interface perturbations utilizing the standard 2-D approach.

THIS PAGE INTENTIONALLY LEFT BLANK

TABLE OF CONTENTS

I.	INTRODUCTION.....	1
A.	PROBLEM STATEMENT	3
B.	PURPOSE STATEMENT.....	4
II.	THEORY	5
A.	REVIEW OF PAST RESEARCH AND ANALYTICAL TOOLS DEVELOPED.....	5
B.	DERIVATION OF PE EQUATIONS FOR THE 3-D SCATTERING MODEL	8
III.	NUMERICAL IMPLEMENTATION	15
A.	HYBRID IMPLEMENTATION USING A TRI-DIAGONAL SOLUTION FOR THE SCATTERING TERM	15
B.	DEFINITION OF ROUGH SURFACE PERTURBATIONS	22
IV.	MODEL RESULTS	29
A.	CONSTANT SLOPE SURFACE VERSUS CONSTANT SLOPE BOTTOM.....	29
1.	Constant Slope Surface and Flat Bottom.....	29
2.	Constant Slope Bottom and a Flat Surface.....	32
3.	Constant Slope Surface Model versus Constant Slope Bottom Model.....	33
B.	CONCENTRIC SINUSOIDAL SURFACE PERTURBATIONS	35
C.	PLANAR SINUSOIDAL SURFACE PERTURBATIONS.....	38
D.	UPWARD SINUSOIDAL SURFACE PERTURBATIONS	40
E.	DOWNWARD SINUSOIDAL SURFACE PERTURBATIONS.....	43
F.	COMPARISON OF THE EFFECT OF 3-D VERSUS $N \times 2$-D	46
1.	Constant Slope Surface Perturbations.....	46
2.	Downward Sinusoidal Surface Perturbations	49
V.	CONCLUSIONS AND FUTURE WORK	53
	LIST OF REFERENCES	55
	INITIAL DISTRIBUTION LIST	57

THIS PAGE INTENTIONALLY LEFT BLANK

LIST OF FIGURES

Figure 1.	Constant-slope surface perturbations.	23
Figure 2.	Concentric sinusoidal surface perturbations.	24
Figure 3.	Planar sinusoidal surface perturbations.	25
Figure 4.	Upward sinusoidal surface perturbations.	27
Figure 5.	Downward sinusoidal surface perturbations.	28
Figure 6.	0-degree radial for a source at depth of 50 m.	30
Figure 7.	180-degree radial for a source at depth of 50 m.	30
Figure 8.	Transmission loss pattern at source depth.	31
Figure 9.	Constant slope surface effect on the waves emitted by a 50 m deep source. ..	31
Figure 10.	0-degree radial for a source at depth of 30 m.	32
Figure 11.	180-degree radial for a source at depth of 30 m.	33
Figure 12.	Model solutions for the water-bottom interface: (left) the constant slope surface; (right) the constant slope bottom.	34
Figure 13.	Transmission loss at water-bottom interface along the 0 radial.	34
Figure 14.	Transmission loss at water-bottom interface along the 180 radial.	35
Figure 15.	0-degree radial for a source at depth of 30 m.	36
Figure 16.	180-degree radial for a source at depth of 30 m.	36
Figure 17.	Transmission loss pattern at source depth.	37
Figure 18.	Concentric sinusoidal surface perturbations effect on a transmission loss field extracted at source depth.	37
Figure 19.	0-degree radial for a source at depth of 30 m.	38
Figure 20.	180-degree radial for a source at depth of 30 m.	38
Figure 21.	Transmission loss pattern at source depth.	39
Figure 22.	Planar sinusoidal surface perturbations effect on a transmission loss field extracted at source depth.	40
Figure 23.	0-degree radial for a source at depth of 30 m.	41
Figure 24.	180-degree radial for a source at depth of 30 m.	41
Figure 25.	Transmission loss pattern at source depth of 30 m.	42
Figure 26.	Upward sinusoidal surface perturbations effect on a transmission loss field extracted at source depth.	42
Figure 27.	0-degree radial for a source at depth of 30 m.	44
Figure 28.	180-degree radial for a source at depth of 30 m.	44
Figure 29.	Transmission loss pattern at source depth.	45
Figure 30.	Downward sinusoidal surface perturbations effect on a transmission loss field extracted at source depth.	45
Figure 31.	Model solutions for the constant slope surface perturbations along the 0 radial: (left) using the basic 2D interface perturbations model; (right) using the 3D model.	47
Figure 32.	Model solutions for the constant slope surface perturbations along the 180 radial: (left) using the basic 2D interface perturbations model; (right) using the 3D model.	47

Figure 33.	The wave pattern results for a 50 m deep source: (left) using the basic 2D interface perturbations model; (right) using the 3D model.....	48
Figure 34.	Model solutions for the constant slope surface perturbations effect on a 50 m deep source waves: (left) using the basic 2D interface perturbations model; (right) using the 3D model.....	48
Figure 35.	Difference in transmission loss values at a constant depth.....	49
Figure 36.	Model solutions for the downward sinusoidal surface perturbations along the 0 radial: (left) using the basic 2D interface perturbations model; (right) using the 3D model.	50
Figure 37.	Model solutions for the downward sinusoidal surface perturbations along the 180 radial: (left) using the basic 2D interface perturbations model; (right) using the 3D model.....	50
Figure 38.	The wave pattern results for a 30 m deep source: (left) using the basic 2D interface perturbations model; (right) using the 3D model.....	51
Figure 39.	Model solutions for the downward sinusoidal surface perturbations on a 30 m depth source waves: (left) using the basic 2D interface perturbations model; (right) using the 3D model.....	51
Figure 40.	Difference in transmission loss values at a constant depth.....	52

LIST OF ACRONYMS AND ABBREVIATIONS

FD	Finite Difference
MMPE	Monterey-Miami Parabolic Equation
PE	Parabolic Equation
SAW	Scattered Acoustic Waves
SPE	Standard Parabolic Equation
SSF	Split-Step Fourier
WAPE	Wide Angle Parabolic Equation

THIS PAGE INTENTIONALLY LEFT BLANK

ACKNOWLEDGMENTS

First and foremost, I would like to thank Professor Kevin Smith for his guidance and the use of his model on which my entire thesis is based and for his assistance in the use of the model.

Second, I would like to thank my wife, Sara, for enduring the long nights and stress she has taken for me to reach this point; without her support and encouragement I would not be who I am today. Also I would like to thank my daughter, Tulai, who kept me inspired, and my parents because they always believed in me and gave me wings. Thank you all for supporting me during these hard days; I am very proud of you, and I love you.

Last but not least, I would like to thank the professors of my department for their valuable input throughout the whole period.

THIS PAGE INTENTIONALLY LEFT BLANK

I. INTRODUCTION

In reality, all surfaces are rough, and it is often important to know how surface roughness changes the properties of scattered acoustic waves (SAW) compared with those reflected from a plane surface. The extent to which surface roughness affects wave scattering and finally the way it propagates is therefore of great interest. Over the last few decades this problem has received considerable attention in several branches of physics, meteorology and engineering. Of major interest has been the study of electromagnetic wave scattering from rough surfaces, which has been crucial in designing many different operational systems (e.g., radar systems) where the effects of the roughness of the land and sea surfaces on signals have been studied (e.g., Ogilvy 1987). Similarly, considerable interest has been concentrated on the interaction of sound waves with rough surfaces owing to its significance in several fields. Rough-surface effects on the acoustics field have been extensively studied as well (e.g., Chimenti and Lobmis 1998).

Acoustics, generally speaking, is one of the primary means by which the underwater environment can be sampled, because acoustic waves are used in the underwater medium in much the same way that electromagnetic waves are used in the atmosphere. The propagation of acoustic waves in the underwater environment is important for several areas, including navigation, ocean observation, detection of submerged objects, and real-time underwater communications. As the ocean environment changes, the refraction and scattering of the acoustic field is affected. Over long time and space scales, the change in the characteristics of the sea-water throughout the water column causes the sound speed profile to change. This in turn shifts the acoustic paths and changes the overall capacity for the ocean to transmit acoustic waves.

Modulating a pressure-release ocean surface over short time and range scales has been found to be more efficient in studying the acoustic paths in which virtually all incident acoustic energy is reflected in the water column (Medwin and Clay 1998). Consequently, multi-paths will be generated as long as the surface modulates over time and space (Senne 2012).

Certainly, there are numerous environmental factors that can influence the acoustic wave propagation in the ocean, such as water temperature and salinity, as well as sea bottom and surface perturbations. The impact of all these factors on acoustic wave propagation are studied in order to determine the performance level of underwater acoustic systems and also to develop techniques for using acoustic signals to measure the physical parameters of the ocean. Surface roughness is just one among several environmental parameters that can have noticeable and essential influence on underwater acoustic propagation.

Biot's 1957 paper suggested one way to approach the study of the scattering of acoustic waves from a rough surface. The idea was to treat the surface as a collection of hemispherical protuberances—or “bosses.” He states:

A simple solution is developed for the reflected waves on a rough surface from a simple harmonic point source. It is assumed that the roughness is represented by a distribution of hemispherical bosses whose size and mutual distance are small relative to the wavelength. It is shown that under these conditions the effect of the roughness is equivalent to a boundary condition for the wave equation. This boundary condition embodies the surface polarization and the mutual interaction of the bosses.

Until recently, only 2-D models have been implemented in order to compute and illustrate the rough surface effects upon the acoustic radials within the field (e.g., Shchegrov 1995). More recent 3-D modeling of rough surface scattering has been based on ray models or localized calculations of full-field scattering. As full field approximations provide more information than ray path solutions, a parabolic equation (PE) approximation is chosen to model the acoustic field out to long range with many multipath contributions from bottom and surface scattering.

In this study, a three dimensional (3-D) ocean acoustic model has been combined with a 2-D rough surface formulation of a parabolic equation model to simulate the effects of sea surface roughness on acoustic wave propagation with multiple surface interactions. Rough sea surface realizations are generated in the acoustic model. An approach to achieve high resolution and accurate results while maintaining computational

efficiency is applied. The results of the scattering calculations are then compared with results from the simple 2-D model.

Throughout this thesis, the PE model is used to determine the acoustic field at a variety of range and depth locations in an underwater environment. The second chapter reviews the past research and the analytical tools developed. It also includes the derivation of the PE equations for the 3-D scattering model approach and a description of its usage - including the treatment of rough sea surfaces. Concerning the numerical implementations, Chapter III introduces the hybrid implementation for the scattering term using a tri-diagonal solution in addition to defining the rough surface perturbation equations that are required for the solution. Results from this acoustic model are presented in Chapter IV, which includes an accounting of the field study through different surface perturbations by introducing five separate models while analyzing the effects of rough surface on acoustic propagation for each model. The PE model coupled with each type of 3-D scattering model is compared against previous 2-D model results in Chapter IV.

A. PROBLEM STATEMENT

The intensity range of the reflected waves can vary widely due to the impact of the evolving sea surface over a short time scale (Ogilvy 1987). Generally, acoustic waves scatter from surfaces with wavelengths that are comparable to or larger than the acoustic wavelength. As the acoustic wave frequency increases, the associated acoustic wavelength decreases. Consequently, smaller scales of roughness at the boundaries become more important. This is a key point when considering sea surface modeling. Sea surfaces are made up of a variety of wave amplitudes and wavelengths that are superimposed. Depending on the acoustic frequency being used, several of these individual surface wave components may play important roles in affecting the acoustic wave. For example, high frequencies, upon which acoustic communication systems depend, are more susceptible to small fluctuations in the sea surface roughness (Senne 2012).

The importance of the 3-D out-of-plane models has been suggested by Karjadi (2011), as he states:

Although the present 2-D acoustic model provides a simple and computationally efficient technique of examining the fluctuations of arrival times and angles caused by surface waves, the 2-D approach does not directly address the out-of-plane scattering caused by surface waves; to properly model these out-of-plane scattering effects, a full 3-D acoustic wave model is required.

Moreover, Senne (2012) has discussed the importance of the realistic evolving rough sea surface by stating:

Understanding acoustic interactions in the vicinity of the rough sea surface and maximizing the usability of underwater communication systems can be achieved through the modeling of acoustic propagation within realistic ocean environments that include time-varying rough sea surfaces.

B. PURPOSE STATEMENT

The goal of the present work is to realize the general effects of the environment variability, such as rough surface scatter, on the 3-D propagation which is critical in evaluating the limitations of existing sonar prediction models. If the 3-D effects are found to be significant, this suggests sonar prediction models must be adapted to account for these effects.

In Chapter II, the selected 2-D and 3-D techniques for rough surface scattering calculations are introduced along with a description of how the two models are integrated.

Comparisons between this model output and the output of basic 2-D interface perturbation models are considered to show the feasibility of the approach and demonstrate the ability of the model to track acoustic wave propagation under fluctuating sea surfaces from one range step to another.

II. THEORY

A theoretical procedure using a full 3-D PE model is developed in an effort to solve the acoustic propagation problem at the surface of the ocean in the presence of surface displacements. This theory is believed to be an improvement over past efforts that computed the effects of rough surface scattering using simple models that were applied in 2-D only.

A. REVIEW OF PAST RESEARCH AND ANALYTICAL TOOLS DEVELOPED

We discuss briefly here each of the major techniques which have been applied to the issue of rough surface scattering. Due to the subject importance to the various scientific fields, there are numerous papers related to rough surface scattering. We have selected a representative sample in order to introduce previous techniques used and the analytical tools developed.

Probably the first reported work on scattering from rough surfaces was by Rayleigh (1878) who discussed the scattering of a normally incident sound wave by a corrugated (sinusoidal) surface separating two acoustic media. He assumed that the scattered field could be written as a sum of plane waves travelling away from the rough surface. This approach has since been extended by other authors to non-normal incidence and to random rough surfaces (Ogilvy 1987).

In the perturbation approach, the rough surface is regarded as a perturbation to a smooth plane, and the consequent change in the scattering coefficient which measures how much of the incident acoustic waves are scattered, due to the presence of roughness, is calculated. This approach requires that the height deviation of the surface away from the smooth plane is everywhere small compared to the wavelength of the incident wave. In addition, the slope of the surface must be small in comparison to unity (Gilbert and Knopoff 1960).

Undoubtedly the approach most prevalent in the literature is the tangent plane, or Kirchhoff, method. Probably the first use of this theory was by Eckart (1953), applied to acoustic wave scattering, and Davies (1955) for electromagnetic wave scattering. Here the scattering surface is assumed to be everywhere sufficiently smooth so that the reflection properties of any point on the surface are those of a plane passing through that point, parallel to the local tangent to the surface. This method leads to a restriction on the rate of change of the surface gradient but no direct restriction on the magnitude of the surface height or surface gradient (Ogilvy 1987).

A number of studies have considered the mechanisms governing interactions between underwater acoustics and rough sea surfaces. When acoustic waves interact with a perfectly flat sea surface, they reflect from that surface just as light would reflect from a mirror. That is to say, all reflected energy is directed in the specular direction. As sea surfaces roughen, the acoustic waves interact with the varying scales of surface roughness, and as a result scatter in a multitude of directions. Acoustic energy is thereby spread into non-specular reflections. The exact reflection parameters are dependent on the relationship between the length scales of surface roughness and the wavelengths of the impacting acoustic waves (Ogilvy 1987).

The exact solution of acoustic waves scattering from a rough sea surface can be determined if the incident acoustic wave is considered to be a plane wave, while the surface is assumed to be infinitely periodic (Holfford 1981).

Real ocean environments consist of a multitude of surface wavelengths and are not typical of these idealized environments. Therefore, a variety of scattering models have been utilized in the literature to approximate the interactions between acoustic waves and rough sea surfaces. Historically speaking, the Kirchhoff and perturbation methods have been the most prevalent. The Kirchhoff method is used whenever the acoustic wavelength is smaller than the radius of curvature of the surface. This limits the Kirchhoff approximation to being primarily applied to high acoustic frequencies. Because the Kirchhoff formulation treats all points of the scattered field on the rough surface as being locally flat, the approximation provides a series of reflections from different points along the surface. The perturbation method assumes the surface is only slightly rough,

and treats the rough surface as a group of perturbations from a smooth surface. As such, it is limited by the allowable magnitudes of surface displacement and surface slope. Whereas the Kirchhoff method is used primarily for high acoustic frequencies, the perturbation method is used mostly for low acoustic frequencies, whose wavelengths are generally large in comparison with the surface height (Ogilvy 1987).

More recently, the small-slope approximation has gained in prominence. The small slope approximation was analyzed by Thorsos and Broschat (1995) as a series in generalized surface slope for the pressure-release (Dirichlet) boundary condition. This method was later shown, in its lowest order, to reduce to the perturbation or Kirchhoff approximations within each of their respective regimes (Thorsos and Broschat 1997).

To predict the impulse responses of high frequency acoustics, rough surface scattering is most commonly treated through the application of the previously mentioned scattering models to acoustic ray codes. The main benefit of these ray codes is that they provide a faster calculation scheme than full-field models, such as PE solutions. A lot of work has been done in order to examine the effectiveness of a few surface scattering mechanisms applied to ray approximation models in predicting acoustic returns and found that while the small slope approximation gave the best results, several of the methods yielded inaccurate results when surface roughness increased (Williams, Thorsos, and Elam 2004).

PE models, as an alternative to ray-based models, have long been used by the underwater acoustics community to study sound propagation. By maintaining full-field characteristics, PE models are able to track both the real and imaginary amplitude and phase values of the wave field over the entire water column, giving a total field at all depths and ranges. PE models are also able to track fluctuations in the acoustic channel over short time steps, which enable the calculation of coherence between successive model runs. Implementing rough surfaces into PE models follows a different approach than the ray codes. Rather than calculate the scattering statistics of the rough surface and then use that information to alter the acoustic wave, PE models instead adapt the range-marching scheme to incorporate rough surfaces into the acoustic field (Senne 2012).

The use of PE models for acoustic frequencies that are typical of communications signals has historically been sparse due to the computational effort required. However, recent advances in computer systems have allowed for faster calculations that enable PE methods to be a viable option even at moderate to high acoustic frequencies (Senne 2012).

B. DERIVATION OF PE EQUATIONS FOR THE 3-D SCATTERING MODEL

Following the development of Smith (2012), we begin with a 3-D version of the standard PE approximation in Cartesian coordinates,

$$\frac{\partial \Psi}{\partial x} = -ik_o(T_{op} + U_{op})\Psi \quad , \quad z > \eta(x, y) \quad (1)$$

where Ψ is the PE “field function,” and T_{op} and U_{op} are the “kinetic” and “potential” energy operators of the PE Hamiltonian. Using the Standard Parabolic Equation (SPE) approximation (e.g., Smith 2001), these operators are defined in three dimensions as

$$T_{op} = T_{3DSPE} = -\frac{1}{2k_o^2} \frac{\partial^2}{\partial z^2} - \frac{1}{2k_o^2} \frac{\partial^2}{\partial y^2} \quad , \quad \text{and} \quad U_{op} = U_{3DSPE} = -\frac{1}{2}(n^2 - 1). \quad (2)$$

The rough surface boundary condition is introduced by defining the location of the pressure release rough surface at depth

$$z = \eta(x, y). \quad (3)$$

The pressure release condition then requires

$$\Psi(z = \eta(x, y), x, y) = 0. \quad (4)$$

Introducing an image field above the surface produces odd symmetry in the field about the pressure release boundary which must now satisfy

$$\Psi(-z + 2\eta(x, y), x, y) = -\Psi(z, x, y). \quad (5)$$

Thus, the image ocean must satisfy the SPE of the form

$$\frac{\partial \Psi}{\partial x} + 2 \frac{\partial \eta}{\partial x} \frac{\partial \Psi}{\partial z} = -ik_o (T_{3DSPE} + U_{3DSPE}) \Psi \quad , \quad z < \eta(x, y). \quad (6)$$

Tappert and Nghiem-Phu (1985) introduced a field transformation

$$\Psi(z, x, y) = \begin{cases} \tilde{\Psi}(z, x, y) & , \quad z > \eta(x, y) \\ e^{-i2k_o \frac{\partial \eta}{\partial x} (z - \eta)} \tilde{\Psi}(z, x, y) & , \quad z < \eta(x, y). \end{cases} \quad (7)$$

In the real ocean, this transformation produces

$$\frac{\partial \tilde{\Psi}}{\partial x} = -ik_o (T_{3DSPE} + U_{3DSPE}) \tilde{\Psi} \quad , \quad z > \eta(x, y). \quad (8)$$

In the image ocean, we must first evaluate the left-hand side of that image ocean form mentioned previously in Eq. (6)

$$\begin{aligned} & \frac{\partial \Psi}{\partial x} + 2 \frac{\partial \eta}{\partial x} \frac{\partial \Psi}{\partial z} \\ &= e^{-i2k_o \frac{\partial \eta}{\partial x} (z - \eta)} \left\{ \frac{\partial \tilde{\Psi}}{\partial x} - i2k_o \frac{\partial^2 \eta}{\partial x^2} (z - \eta) \tilde{\Psi} - i2k_o \left(\frac{\partial \eta}{\partial x} \right)^2 \tilde{\Psi} + 2 \frac{\partial \eta}{\partial x} \frac{\partial \tilde{\Psi}}{\partial z} \right\}. \end{aligned} \quad (9)$$

The right-hand side of Eq. (6) includes the operator

$$T_{3DSPE} = -\frac{1}{2k_o^2} \frac{\partial^2}{\partial z^2} - \frac{1}{2k_o^2} \frac{\partial^2}{\partial y^2}, \quad (10)$$

so

$$\begin{aligned} T_{3DSPE} \Psi &= -\frac{1}{2k_o^2} e^{-i2k_o \frac{\partial \eta}{\partial x} (z - \eta)} \left\{ \left[\frac{\partial^2 \tilde{\Psi}}{\partial z^2} - i4k_o \frac{\partial \eta}{\partial x} \frac{\partial \tilde{\Psi}}{\partial z} - 4k_o^2 \left(\frac{\partial \eta}{\partial x} \right)^2 \tilde{\Psi} \right] \right. \\ &\quad \left. + \frac{\partial^2 \tilde{\Psi}}{\partial y^2} - i4k_o \left(\frac{\partial^2 \eta}{\partial x \partial y} (z - \eta) - \frac{\partial \eta}{\partial x} \frac{\partial \eta}{\partial y} \right) \frac{\partial \tilde{\Psi}}{\partial y} \right. \\ &\quad \left. - i2k_o \left(\frac{\partial^3 \eta}{\partial x \partial y^2} (z - \eta) - 2 \frac{\partial^2 \eta}{\partial x \partial y} \frac{\partial \eta}{\partial y} - \frac{\partial \eta}{\partial x} \frac{\partial^2 \eta}{\partial^2 y} - i2k_o \left(\frac{\partial^2 \eta}{\partial x \partial y} (z - \eta) - \frac{\partial \eta}{\partial x} \frac{\partial \eta}{\partial y} \right)^2 \right) \tilde{\Psi} \right\}. \end{aligned} \quad (11)$$

After combining the right-hand side with the left-hand side, we get

$$\begin{aligned}
\frac{\partial \tilde{\Psi}}{\partial x} = & -ik_o \left\{ -\frac{1}{2k_o^2} \left(\frac{\partial^2 \tilde{\Psi}}{\partial z^2} + \frac{\partial^2 \tilde{\Psi}}{\partial y^2} \right) + \left[U_{3DSPE} - 2 \frac{\partial^2 \eta}{\partial x^2} (z - \eta) \right] \tilde{\Psi} \right. \\
& + \frac{i2}{k_o} \left[\frac{\partial^2 \eta}{\partial x \partial y} (z - \eta) - \frac{\partial \eta}{\partial x} \frac{\partial \eta}{\partial y} \right] \frac{\partial \tilde{\Psi}}{\partial y} \\
& + \frac{i}{k_o} \left[\frac{\partial^3 \eta}{\partial x \partial y^2} (z - \eta) - 2 \frac{\partial^2 \eta}{\partial x \partial y} \frac{\partial \eta}{\partial y} \right. \\
& \left. \left. - \frac{\partial \eta}{\partial x} \frac{\partial^2 \eta}{\partial y^2} - i2k_o \left(\frac{\partial^2 \eta}{\partial x \partial y} (z - \eta) - \frac{\partial \eta}{\partial x} \frac{\partial \eta}{\partial y} \right)^2 \right] \tilde{\Psi} \right\}.
\end{aligned} \tag{12}$$

Consequently, we can combine these expressions together into a single formulation,

$$\frac{\partial \tilde{\Psi}}{\partial x} = -ik_o (\tilde{T}_{op} + \tilde{U}_{op}) \tilde{\Psi} \tag{13}$$

with

$$\tilde{T}_{op} = \begin{cases} T_{3DSPE} & , z > \eta(x, y) \\ T_{3DSPE} + \frac{i2}{k_o} \left[\frac{\partial^2 \eta}{\partial x \partial y} (z - \eta) - \frac{\partial \eta}{\partial x} \frac{\partial \eta}{\partial y} \right] \frac{\partial}{\partial y} & , z < \eta(x, y) \end{cases} \tag{14}$$

and

$$\tilde{U}_{op} = \begin{cases} U_{3DSPE} & , z > \eta(x, y) \\ U_{3DSPE} - 2 \frac{\partial^2 \eta}{\partial x^2} (z - \eta) \\ + \frac{i}{k_o} \left[\frac{\partial^3 \eta}{\partial x \partial y^2} (z - \eta) - 2 \frac{\partial^2 \eta}{\partial x \partial y} \frac{\partial \eta}{\partial y} - \frac{\partial \eta}{\partial x} \frac{\partial^2 \eta}{\partial y^2} - i2k_o \left(\frac{\partial^2 \eta}{\partial x \partial y} (z - \eta) - \frac{\partial \eta}{\partial x} \frac{\partial \eta}{\partial y} \right)^2 \right] & , z < \eta(x, y) \end{cases} \tag{15}$$

The previously mentioned equations represent an exact formulation of the 3-D rough surface scattering utilizing the SPE approximation, as originally derived by Smith (2012). The form of the 3-D kinetic energy operator introduces some computational complexities. Specifically, the field above the interface undergoes a separate cross-range operator. And while it is possible to apply this operator, it is not possible to apply it at a single depth mesh point since the rough surface varies with cross-range (i.e., $\eta(x, y_m) \neq \eta(x, y_n)$).

In order to overcome this difficulty, an approach has been suggested by Smith (2013). First, at each range step (x_i), the 3-D field is transformed from cross-range spatial variable (y) to cross-range wavenumber variable (k_y) over all depths. Concurrently, transformation from depth variable (z) to vertical wavenumber variable (k_z) should also be performed. Second, a copy of the field in (k_y, k_z) space should be implemented. Third, to one copy of the field, the \tilde{T}_{op} for $z > \eta$ should be applied, while to the other copy the \tilde{T}_{op} for $z < \eta$ should be applied. Fourth, each copy is transformed back to the spatial (y, z) domain. Fifth, based on the local surface height at range (x_i), and for each cross-range (y_m), the appropriate form of the field should be recombined. Finally, the appropriate form of \tilde{U}_{op} should then be applied to complete the range step to (x_{i+1}).

The preceding 3-D expressions were developed using the SPE approximation in Cartesian coordinates (x, y, z). The development of the equations in cylindrical coordinates (r, θ, ϕ) closely follows the previous approach, beginning with

$$\frac{\partial \Psi}{\partial r} = -ik_o(T_{op} + U_{op})\Psi \quad , \quad z > \eta(r, \phi) \quad , \quad (16)$$

where

$$T_{op} = T_{3DSPE} = -\frac{1}{2k_o^2} \frac{\partial^2}{\partial z^2} - \frac{1}{2k_o^2 r^2} \frac{\partial^2}{\partial \phi^2} \quad , \quad U_{op} = U_{3DSPE} = -\frac{1}{2}(n^2 - 1). \quad (17)$$

This time the rough surface boundary condition is introduced by defining the location of the pressure release rough surface at depth

$$z = \eta(r, \phi). \quad (18)$$

Then the pressure release boundary condition is defined by

$$\Psi(z = \eta(r, \phi), r, \phi) = 0. \quad (19)$$

Introducing an image field for $z < \eta$ produces the symmetry defined by

$$\Psi(-z + 2\eta(r, \phi), r, \phi) = -\Psi(z, r, \phi). \quad (20)$$

Thus, the image ocean must satisfy a PE of the form

$$\frac{\partial \Psi}{\partial r} + 2 \frac{\partial \eta}{\partial r} \frac{\partial \Psi}{\partial z} = -ik_o (T_{op} + U_{op}) \Psi \quad , z < \eta(r, \phi). \quad (21)$$

As before, we introduce a field transformation of the form

$$\Psi(z, r, \phi) = \begin{cases} \tilde{\Psi}(z, r, \phi) & , z > \eta(r, \phi) \\ e^{-i2k_o \frac{\partial \eta}{\partial r} (z - \eta)} \tilde{\Psi}(z, r, \phi) & , z < \eta(r, \phi). \end{cases} \quad (22)$$

These equations follow exactly the same development as before, but now we end up with the combined formulation

$$\frac{\partial \tilde{\Psi}}{\partial r} = -ik_o(\tilde{T}_{op} + \tilde{U}_{op})\tilde{\Psi} \quad (23)$$

with

$$\tilde{T}_{op} = \begin{cases} T_{3DSPE} & , z > \eta(r, \phi) \\ T_{3DSPE} + \frac{i2}{k_o r^2} \left[\frac{\partial^2 \eta}{\partial r \partial \phi} (z - \eta) - \frac{\partial \eta}{\partial r} \frac{\partial \eta}{\partial \phi} \right] \frac{\partial}{\partial \phi} & , z < \eta(r, \phi) \end{cases} \quad (24)$$

and

$$\tilde{U}_{op} = \begin{cases} U_{3DSPE} & , z > \eta(r, \phi) \\ U_{3DSPE} - 2 \frac{\partial^2 \eta}{\partial r^2} (z - \eta) \\ + \frac{i}{k_o r^2} \left[\frac{\partial^3 \eta}{\partial r \partial \phi^2} (z - \eta) - 2 \frac{\partial^2 \eta}{\partial r \partial \phi} \frac{\partial \eta}{\partial \phi} - \frac{\partial \eta}{\partial r} \frac{\partial^2 \eta}{\partial \phi^2} - i2k_o \left(\frac{\partial^2 \eta}{\partial r \partial \phi} (z - \eta) - \frac{\partial \eta}{\partial r} \frac{\partial \eta}{\partial \phi} \right)^2 \right] & , z < \eta(r, \phi) \end{cases} \quad (25)$$

The implementation of these equations follows the same outline as provided in the Cartesian coordinates approach.

However, it has been shown (Smith and Colosi 2008) that the SPE approximation performs poorly in 3-D coordinates since cross-ranges separated from the center introduce lateral angles that are not well treated. They suggest that a better approach in 3-D is to utilize the 2-D wide-angle parabolic equation (WAPE) approximation in order to produce the proper 3-D structure of the field. It is shown that several problems in sound propagation cannot be studied by using a small-angle parabolic equation, and need a WAPE for their solution (Ostashev and Blanc-Benon 1997).

Smith (2012) discussed the approach to these scattering corrections using a wide-angle PE. He noted that the same scattering corrections result if third order derivatives of the field and surface slope are ignored. Therefore, we shall utilize the 3-D WAPE propagator functions with the scattering correction terms derived previously. These operators are defined in cylindrical coordinates by

$$T_{op} = T_{3DWAPE} = 1 - \sqrt{1 + \frac{1}{k_o^2} \frac{\partial^2}{\partial z^2} + \frac{1}{k_o^2 r^2} \frac{\partial^2}{\partial \phi^2}}, \quad U_{op} = U_{3DWAPE} = -(n-1). \quad (26)$$

Meanwhile, the WAPE introduces new terms which depend upon vertical derivatives of the field of second order and higher and/or products with terms that are second order and higher factors of the surface slope. Even though the WAPE implementation in the water column allows for better accuracy of high angle propagation, the existing application of the rough surface scattering approach does not appear to support the same level of high angle scattering and assumes small surface slopes.

An approximation is done to the \tilde{U}_{op} in the image ocean by dropping the third order and higher terms in the derivative of the surface displacement that neglects the effects of very high slopes in the scattering and the third order and higher azimuthal derivatives that invoke a small-angle approximation. However, second order derivative terms are maintained. This is consistent with second order derivatives of the propagating field, although such terms are not difficult to include.

III. NUMERICAL IMPLEMENTATION

A. HYBRID IMPLEMENTATION USING A TRI-DIAGONAL SOLUTION FOR THE SCATTERING TERM

The forms of the derived equations using cylindrical or Cartesian coordinates are identical with the obvious substitution

$$\frac{\partial}{\partial y} \rightarrow \frac{1}{r} \frac{\partial}{\partial \varphi}. \quad (27)$$

For conciseness, we shall only consider the Cartesian form in what follows, although the model implementation is done using cylindrical coordinates.

The derived equations in the previous chapter contained the additional term in the \tilde{T}_{op} operator for $z < \eta(x, y)$ which cannot be applied in the k_y wavenumber domain, as is traditionally done for \tilde{T}_{op} . Specifically, if we write

$$\tilde{T}_{op} = \begin{cases} T_{3DWAPE} & , z > \eta(x, y) \\ T_{3DWAPE} + R \frac{\partial}{\partial y} & , z < \eta(x, y) , \end{cases} \quad (28)$$

we see that $T_{3DWAPE} = T_{3DWAPE} \left(\frac{\partial^2}{\partial y^2}, \frac{\partial^2}{\partial z^2} \right)$, which can be applied in the (k_y, k_z) wavenumber

domain. However, $R \frac{\partial}{\partial y} = R(x, y, z) \frac{\partial}{\partial y}$ cannot be treated so easily.

It is the combined dependence of $R \frac{\partial}{\partial y}$ on both y and $\frac{\partial}{\partial y}$ (or φ and $\frac{\partial}{\partial \varphi}$ in the cylindrical coordinates) that does not allow a simple implementation via a Split-Step Fourier (SSF) algorithm. Instead, the following hybrid approach is proposed.

Loosely following the approach of Yevick and Thomson (1997), we will focus on the image field evolution equation

$$\frac{\partial \tilde{\Psi}}{\partial x} = -ik_o \tilde{H}_{op} \tilde{\Psi} , \quad (29)$$

where, \tilde{H}_{op} is a Hamiltonian-like operator that defines the evolution of the PE field function in range. We may then use the approximate marching algorithm solution

$$\tilde{\Psi}(x + \Delta x) = e^{-ik_o \Delta x \tilde{H}_{op}(r)} \tilde{\Psi}(x). \quad (30)$$

Here,

$$\tilde{H}_{op}(x) = \tilde{T}_{op}(x) + \tilde{U}_{op}(x) = R \frac{\partial}{\partial y} + \tilde{T}_{op} + \tilde{U}_{op} , \quad (31)$$

so we may define,

$$\tilde{\Psi}(x + \Delta x) = e^{-ik_o \Delta x R \frac{\partial}{\partial y}} e^{-ik_o \Delta x T_{3D}} e^{-ik_o \Delta x U_{3D}} \tilde{\Psi}(x). \quad (32)$$

Note that this form assumes that the rough surface correction is applied after the kinetic energy operator (T_{3D}).

The Monterey-Miami Parabolic Equation (MMPE) model employs a centered-step scheme implementation, which in the real ocean takes the form (Smith and Tappert 1993, Smith 2001)

$$\Psi(x + \Delta x) = e^{-i \frac{1}{2} k_o \Delta x U_{3D}(x + \Delta x)} FFT_{yz}^{-1} \left\{ e^{-ik_o \Delta x \hat{T}_{3D}(k_x, k_y)} FFT_{yz} \left[e^{-i \frac{1}{2} k_o \Delta x U_{3D}} \Psi(x) \right] \right\} , \quad (33)$$

where $\Psi(x) = \Psi(x, y, z)$ and $\hat{T}_{3D}(k_x, k_y)$ is the scalar form of the operator T_{3D} in the (k_y, k_z) wavenumber space.

The image ocean solution can utilize the SSF algorithm for the T_{3D} term, but must employ an alternative method for the $R \frac{\partial}{\partial y}$ term. Thus, we will implement a centered-step scheme defined by

$$\tilde{\Psi}(x + \Delta x) = e^{-i\frac{1}{2}k_o\Delta x\tilde{U}_{3D}(x+\Delta x)} e^{-ik_o\Delta xR(x+\frac{1}{2}\Delta x)\frac{\partial}{\partial y}} FFT_{yz}^{-1} \left\{ e^{-ik_o\Delta x\tilde{T}_{3D}(k_x, k_y)} FFT_{yz} \left[e^{-i\frac{1}{2}k_o\Delta x\tilde{U}_{3D}(x)} \tilde{\Psi}(x) \right] \right\}. \quad (34)$$

In order to implement this equation, we should determine how to apply the operator $e^{-i\zeta R\gamma}$ with $\zeta = k_o\Delta x$ and $\gamma = \frac{\partial}{\partial y}$ by defining the intermediate step solution as

$$\tilde{\Psi}'(x + \Delta x') = FFT_{yz}^{-1} \left\{ e^{-i\delta\tilde{T}_{3D}} FFT_{yz} \left[e^{-i\frac{1}{2}\delta\tilde{U}_{3D}(x)} \tilde{\Psi}(x) \right] \right\}. \quad (35)$$

The final solution at the end of each range step is then obtained from

$$\tilde{\Psi}(x + \Delta x) = e^{-i\frac{1}{2}\zeta\tilde{U}_{3D}(x+\Delta x)} \tilde{\Psi}'(x + \Delta x'), \quad (36)$$

where

$$\tilde{\Psi}(x + \Delta x') = e^{-i\zeta R\gamma} \tilde{\Psi}'(x + \Delta x'). \quad (37)$$

The rough surface correction operator can be represented by the Padé approximant (Collins 1990)

$$e^{-i\zeta R\gamma} \approx \frac{1 - \frac{1}{2}i\zeta R\gamma}{1 + \frac{1}{2}i\zeta R\gamma}, \quad (38)$$

which is valid for small γ , implying small corrections in cross-range scattering at each step. From this approximation, we obtain a finite difference system of equations based upon

$$\left[1 + \frac{1}{2}i\zeta R\gamma\right] \tilde{\Psi}(x + \Delta x') = \left[1 - \frac{1}{2}i\zeta R\gamma\right] \tilde{\Psi}'(x + \Delta x'). \quad (39)$$

This may be written in a vector-matrix form as

$$\bar{A}\tilde{\Psi} = \bar{B}\tilde{\Psi}' = \bar{C}, \quad (40)$$

where

$$\tilde{\Psi} = \begin{bmatrix} \tilde{\Psi}_1 \\ \tilde{\Psi}_2 \\ \tilde{\Psi}_3 \\ \vdots \\ \tilde{\Psi}_N \end{bmatrix} \quad \tilde{\Psi}' = \begin{bmatrix} \tilde{\Psi}'_1 \\ \tilde{\Psi}'_2 \\ \tilde{\Psi}'_3 \\ \vdots \\ \tilde{\Psi}'_N \end{bmatrix}, \quad (41)$$

and $\tilde{\Psi}_n = \tilde{\Psi}(y_n)$, $n=1,2,3,\dots,N$.

The expressions required for the \bar{A} and \bar{B} matrices' components will be based on a 3-point centered approximation to the derivative

$$\gamma\tilde{\Psi} = \frac{\partial\tilde{\Psi}}{\partial y}\bigg|_{y_o} \approx \frac{1}{2\Delta y}(\tilde{\Psi}_1 - \tilde{\Psi}_{-1}), \quad (42)$$

where $\tilde{\Psi}_{\pm 1} = \tilde{\Psi}(y = y_o \pm \Delta y)$. At the end points (n=1 or n=N), we shall invoke the 2-point approximations

$$\gamma\tilde{\Psi} = \frac{\partial\tilde{\Psi}}{\partial y}\bigg|_{y_o} \approx \frac{1}{\Delta y}(\tilde{\Psi}_0 - \tilde{\Psi}_{-1}), \quad (43)$$

$$\gamma\tilde{\Psi} = \frac{\partial\tilde{\Psi}}{\partial y}\bigg|_{y_o} \approx \frac{1}{\Delta y}(\tilde{\Psi}_1 - \tilde{\Psi}_0). \quad (44)$$

The former is used if n=N and the latter applies when n=1.

The matrices may be defined in terms of a_n and b_n where

$$\begin{aligned} \left[1 + \frac{1}{2}i\zeta R\gamma\right]\tilde{\Psi}_o &= \tilde{\Psi}_o + \frac{1}{2}i\zeta R\gamma\tilde{\Psi}_o = \\ \tilde{\Psi}_o + \frac{1}{2}i\zeta R\frac{1}{2\Delta y}(\tilde{\Psi}_1 - \tilde{\Psi}_{-1}) &= \tilde{\Psi}_o + \frac{i\zeta R}{4\Delta y}(\tilde{\Psi}_1 - \tilde{\Psi}_{-1}), \end{aligned} \quad (45)$$

from which we can introduce

$$a_n = \frac{1}{4} \frac{i\zeta R_n}{\Delta y}, \quad b_n = \frac{-1}{4} \frac{i\zeta R_n}{\Delta y}, \quad , R_n = R(y_n). \quad (46)$$

Consequently, we can define two different matrices

$$\bar{A} = \begin{pmatrix} (1-2a_1) & 2a_1 & 0 & 0 & 0 & 0 \\ -a_2 & 1 & a_2 & 0 & 0 & 0 \\ 0 & -a_3 & 1 & a_3 & 0 & 0 \\ 0 & 0 & 0 & \ddots & 0 & 0 \\ 0 & 0 & 0 & -a_{N-1} & 1 & a_{N-1} \\ 0 & 0 & 0 & 0 & -2a_N & (1+2a_N) \end{pmatrix}, \quad (47)$$

and

$$\bar{B} = \begin{pmatrix} (1-2b_1) & 2b_1 & 0 & 0 & 0 & 0 \\ -b_2 & 1 & b_2 & 0 & 0 & 0 \\ 0 & -b_3 & 1 & b_3 & 0 & 0 \\ 0 & 0 & 0 & \ddots & 0 & 0 \\ 0 & 0 & 0 & -b_{N-1} & 1 & b_{N-1} \\ 0 & 0 & 0 & 0 & -2b_N & (1+2b_N) \end{pmatrix}. \quad (48)$$

Now the matrix equation becomes

$$\bar{A}\tilde{\Psi} = \vec{C} = \begin{bmatrix} C_1 \\ C_2 \\ C_3 \\ \vdots \\ C_N \end{bmatrix}, \quad (49)$$

with the elements of \vec{C} are computed from $\bar{B}\tilde{\Psi}$. Equation (50) can be solved by a tri-diagonal matrix algorithm (Press et al. 2007) according to the recursive relations

$$\begin{aligned} \tilde{\Psi}_N &= C'_N \\ \tilde{\Psi}_i &= C'_i - a'_i \tilde{\Psi}_{i+1} \quad , i = 1, 2, 3, \dots, N-2, N-1, \end{aligned} \quad (50)$$

where

$$a'_i = \begin{cases} \frac{2a_1}{1-2a_1} & , i=1 \text{ ,} \\ \frac{a_i}{1+a'_{i-1}a_i} & , i=2,3,\dots,N-1 \text{ ,} \end{cases} \quad (51)$$

$$C'_i = \begin{cases} \frac{C_1}{1-2a_1} & , i=1 \text{ ,} \\ \frac{C_i + C'_{i-1}a_i}{1+a'_{i-1}a_i} & , i=2,3,\dots,N-1 \text{ ,} \\ \frac{C_N + 2a_N C'_{N-1}}{(1+2a_N) + 2a_N a'_{N-1}} & , i=N \text{ .} \end{cases} \quad (52)$$

The outcome of this tri-diagonal matrix solution is then $\tilde{\Psi}(x + \Delta x')$ to which we simply apply the scalar vector multiplier $e^{-i\frac{1}{2}\delta\tilde{U}_{3DSPE}(x+\Delta x)}$ to obtain the solution at the end of the range step $\tilde{\Psi}(x + \Delta x)$.

B. DEFINITION OF ROUGH SURFACE PERTURBATIONS

In order to appropriately test the 3-D scattering model just developed, it is required that we analytically define some simple surface perturbations. In this section, we shall define five simple surface perturbations. These will be defined in cylindrical coordinates, since the model is implemented this way.

First, we define a surface with constant slope in order to determine the way the different radials will be affected by that surface slope using the equation

$$\eta(r, \phi) = 20 + 0.1(r \cos \phi), \quad (53)$$

where $\eta(r, \phi)$ is the surface height with respect to range, r , and the expressions for the required derivatives are then

$$\begin{aligned} \frac{\partial \eta}{\partial r} &= 0.1 \cos(\phi), \\ \frac{\partial^2 \eta}{\partial r^2} &= 0, \\ \frac{\partial \eta}{\partial \phi} &= -0.1r \sin(\phi), \\ \frac{\partial^2 \eta}{\partial r \partial \phi} &= -0.1 \sin(\phi). \end{aligned} \quad (54)$$

This surface is depicted in Fig. 1.

Second, we define the surface roughness for concentric sinusoidal waves

$$\eta(r, \phi) = \sigma \cos(kr), \quad (55)$$

where $\eta(r, \phi)$ is now the surface wave height with respect to range, r (independent of bearing ϕ in this case), σ is the surface wave height amplitude, and k is the surface wavenumber ($2\pi/\lambda_s$ where λ_s is the wavelength of the surface perturbation). Notice here that since the surface does not depend upon the bearing angle, the propagation out along all radials should be affected similarly. Then

$$\begin{aligned}
\frac{\partial \eta}{\partial r} &= -k\sigma \sin(kr), \\
\frac{\partial^2 \eta}{\partial r^2} &= -k^2 \sigma \cos(kr), \\
\frac{\partial \eta}{\partial \phi} &= 0, \\
\frac{\partial^2 \eta}{\partial r \partial \phi} &= 0.
\end{aligned}
\tag{56}$$

This surface is depicted in Fig. 2.

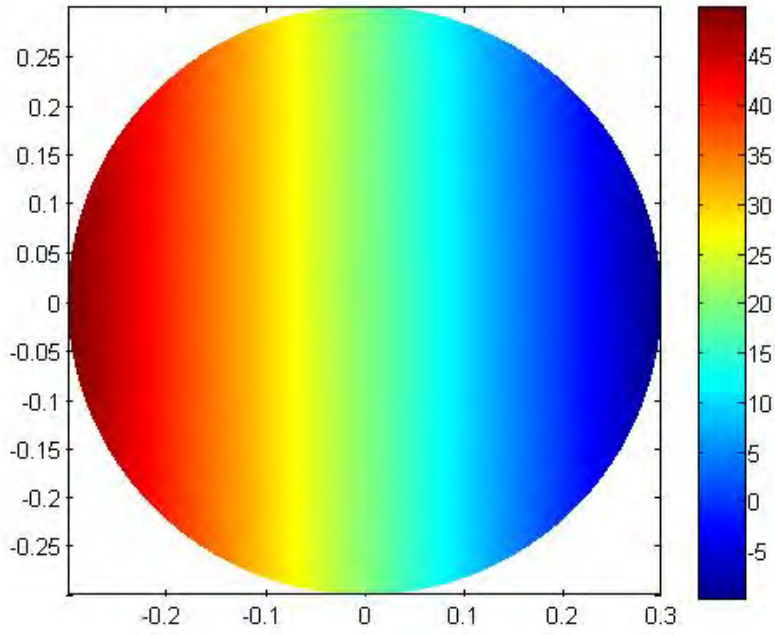


Figure 1. Constant-slope surface perturbations.

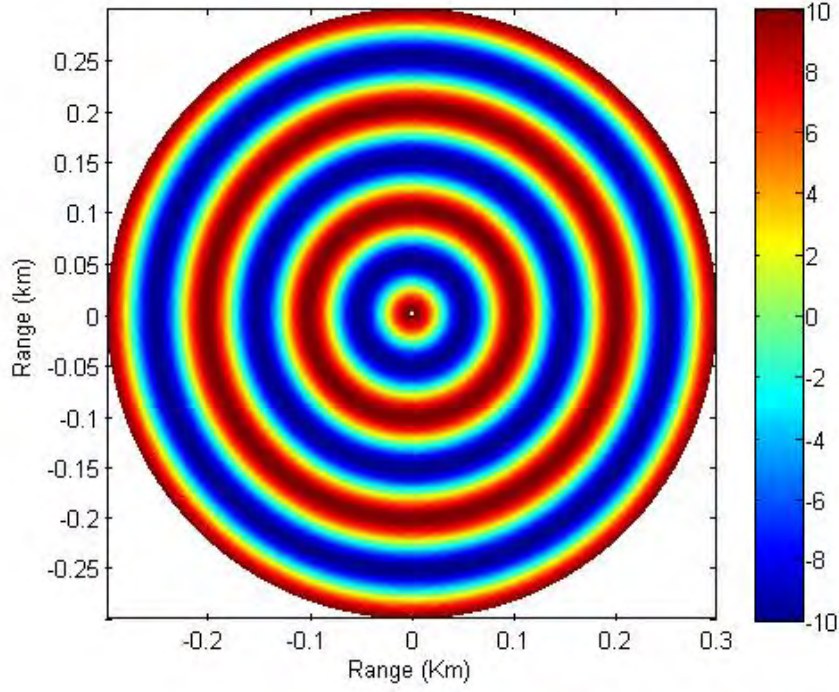


Figure 2. Concentric sinusoidal surface perturbations.

Third, we define the equations introducing the surface roughness for unidirectional sinusoidal waves by

$$\eta(r, \phi) = \sigma \cos(kr \cos \phi), \quad (57)$$

where ϕ is the angle of propagation along each radial. Then

$$\begin{aligned} \frac{\partial \eta}{\partial r} &= -k\sigma \cos(\phi) \sin[kr \cos(\phi)], \\ \frac{\partial^2 \eta}{\partial r^2} &= -\sigma [k \cos(\phi)]^2 \cos[kr \cos(\phi)], \\ \frac{\partial \eta}{\partial \phi} &= kr\sigma \sin(\phi) \sin[kr \cos(\phi)], \\ \frac{\partial^2 \eta}{\partial r \partial \phi} &= k\sigma \sin(\phi) \{ \sin[kr \cos(\phi)] + kr \cos(\phi) \cos[kr \cos(\phi)] \}. \end{aligned} \quad (58)$$

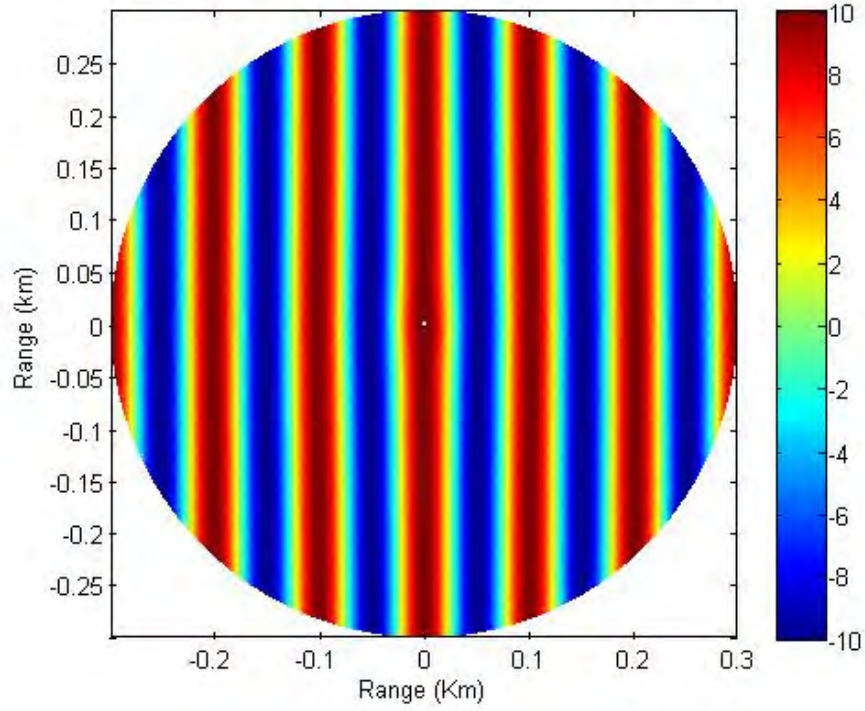


Figure 3. Planar sinusoidal surface perturbations.

Fourth, we define a single upward sinusoidal perturbation on one side only by using the same surface roughness equation as the unidirectional surface waves, but this time we limit the angle of propagation ϕ to be within the forward region of the source and only allow one oscillation,

$$\eta(r, \phi) = \sigma \cos(kr \cos \phi) \quad , \quad \begin{aligned} & -90 < \phi < 90, \\ & r \cos \phi \leq \lambda_s. \end{aligned} \quad (59)$$

Elsewhere, the surface will be constant with a value for $\eta(r, \phi)$ equal to the maximum surface wave height σ . The derivatives in the region of the displacement are then

$$\begin{aligned}
\frac{\partial \eta}{\partial r} &= -k\sigma \cos(\phi) \sin[kr \cos(\phi)], \\
\frac{\partial^2 \eta}{\partial r^2} &= -\sigma[k \cos(\phi)]^2 \cos[kr \cos(\phi)], \\
\frac{\partial \eta}{\partial \phi} &= kr\sigma \sin(\phi) \sin[kr \cos(\phi)], \\
\frac{\partial^2 \eta}{\partial r \partial \phi} &= k\sigma \sin(\phi) \{ \sin[kr \cos(\phi)] + kr \cos(\phi) \cos[kr \cos(\phi)] \},
\end{aligned} \tag{60}$$

while over the other directions and ranges, the sea surface is defined as

$$\begin{aligned}
\eta(r, \phi) &= \sigma, \\
\frac{\partial \eta}{\partial r} &= 0, \\
\frac{\partial^2 \eta}{\partial r^2} &= 0, \\
\frac{\partial \eta}{\partial \phi} &= 0, \\
\frac{\partial^2 \eta}{\partial r \partial \phi} &= 0.
\end{aligned} \tag{61}$$

This surface is depicted in Fig. 4.

Finally, we flip the single upward sinusoidal perturbation wave and shift it until it reaches the mean sea level, where $\eta(r, \phi)$ equals zero everywhere except in the forward region of the source, where the sea surface equation is defined by

$$\eta(r, \phi) = \sigma[1 - \cos(kr \cos \phi)] \quad , \quad \begin{aligned} &-90 < \phi < 90, \\ &r \cos \phi \leq \lambda_s. \end{aligned} \tag{62}$$

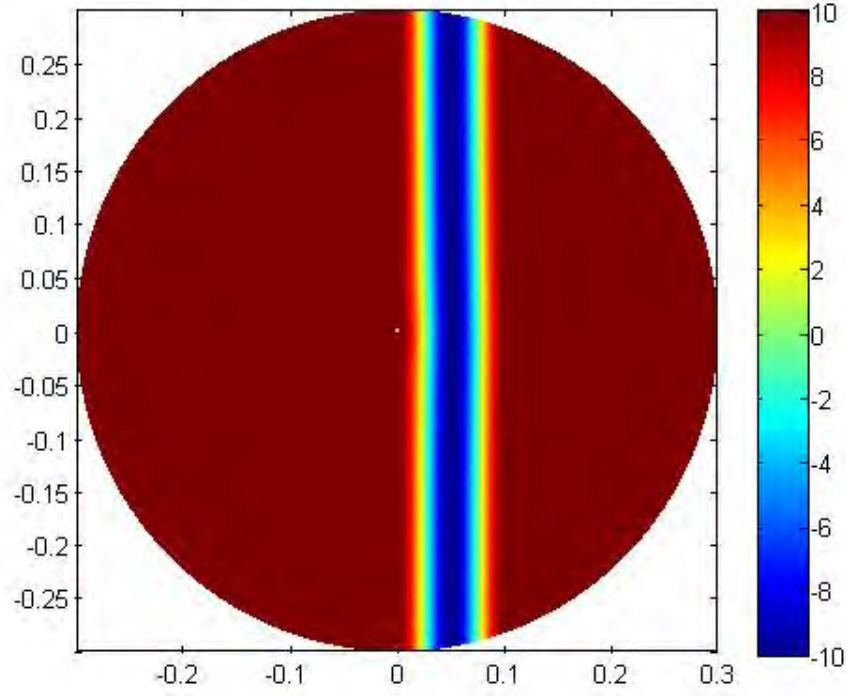


Figure 4. Upward sinusoidal surface perturbations.

The derivatives in the region of the displacement are then

$$\begin{aligned}
 \frac{\partial \eta}{\partial r} &= k\sigma \cos(\phi) \sin[kr \cos(\phi)], \\
 \frac{\partial^2 \eta}{\partial r^2} &= \sigma [k \cos(\phi)]^2 \cos[kr \cos(\phi)], \\
 \frac{\partial \eta}{\partial \phi} &= -kr\sigma \sin(\phi) \sin[kr \cos(\phi)], \\
 \frac{\partial^2 \eta}{\partial r \partial \phi} &= -k\sigma \sin(\phi) \{ \sin[kr \cos(\phi)] + kr \cos(\phi) \cos[kr \cos(\phi)] \}.
 \end{aligned} \tag{63}$$

while all over the other directions, the sea surface is defined as

$$\begin{aligned}
\eta(r, \phi) &= 0, \\
\frac{\partial \eta}{\partial r} &= 0, \\
\frac{\partial^2 \eta}{\partial r^2} &= 0, \\
\frac{\partial \eta}{\partial \phi} &= 0, \\
\frac{\partial^2 \eta}{\partial r \partial \phi} &= 0.
\end{aligned} \tag{64}$$

This surface is depicted in Fig. 5.

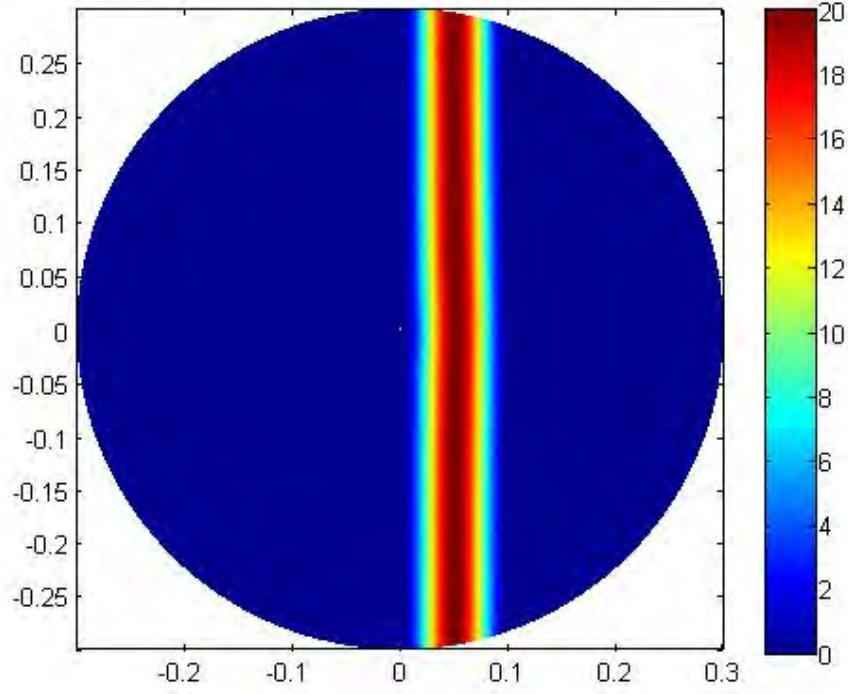


Figure 5. Downward sinusoidal surface perturbations.

IV. MODEL RESULTS

A. CONSTANT SLOPE SURFACE VERSUS CONSTANT SLOPE BOTTOM

Although a sloping surface is a relatively benign definition of a perturbed surface, it does allow a comparison of the rough surface algorithm defined here with a formally equivalent environment defined by a sloping bottom. The solution to a constant slope surface is identical to a constant slope bottom through a simple environmental rotation, assuming ideal point sources in both cases. The approach to the 3-D problem with a non-constant bottom is no different from the approach to the 2-D problem, where the MMPE model simply adjusts the bottom depth at each range step and radial.

1. Constant Slope Surface and Flat Bottom

Solutions to the problem of a sloping surface over a flat bottom are depicted in the following figures. The source is located at a depth of 50 m and the bottom depth is highlighted with a white line at 120 m depth. Figures 6 and 7 display the solutions along opposing radials, with the former along the direction of descending surface depth and the latter along the direction of ascending surface depth. In both cases, the bottom interface is observed to be flat.

In Figure 8, the transmission loss at a single depth, corresponding to the source depth, is extracted from all radials. Note that in the case of a perfectly flat surface and bottom, this would produce concentric rings of interference patterns in the field. In this case, however, the directionality of the propagation along different radials is apparent. Transforming this data to a polar coordinate system produces the results presented in Figure 9. The effect observed is consistent with general expectations of a sloping surface, where the propagation in the direction of the descending surface produces interference patterns compressed in range and, alternatively, the propagation in the direction of the ascending surface produces interference patterns elongated in range.

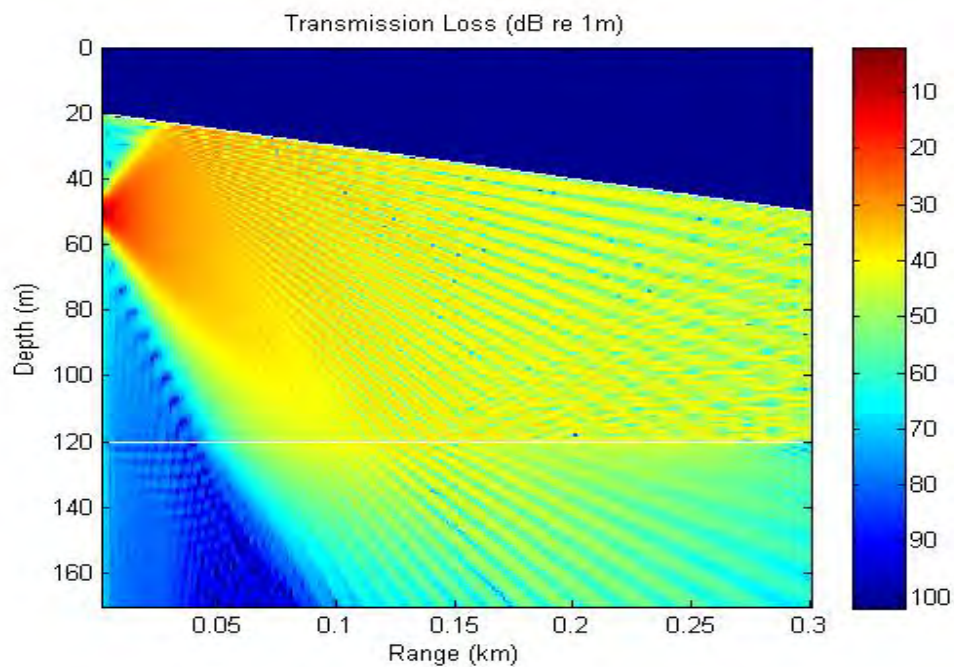


Figure 6. 0-degree radial for a source at depth of 50 m.

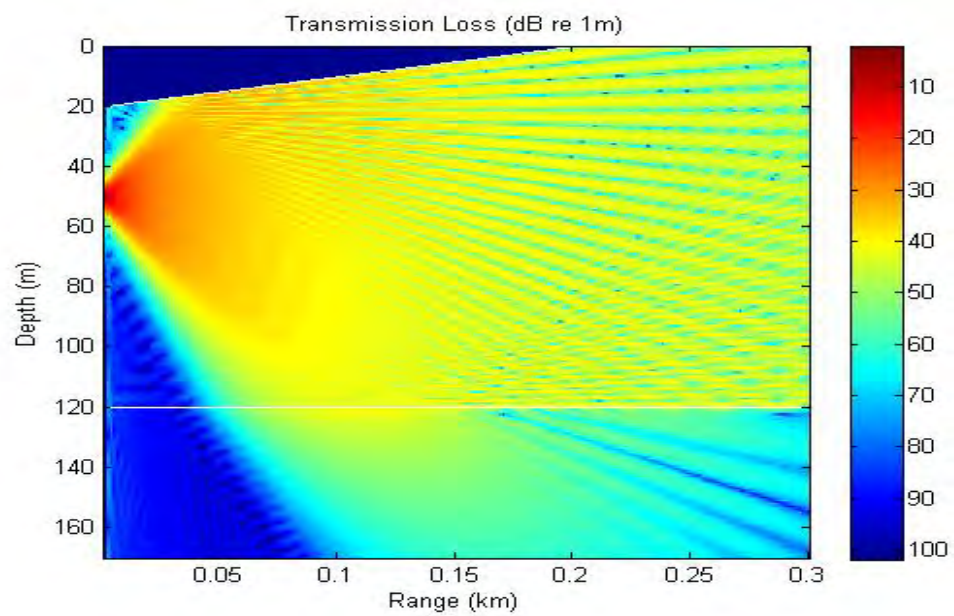


Figure 7. 180-degree radial for a source at depth of 50 m.

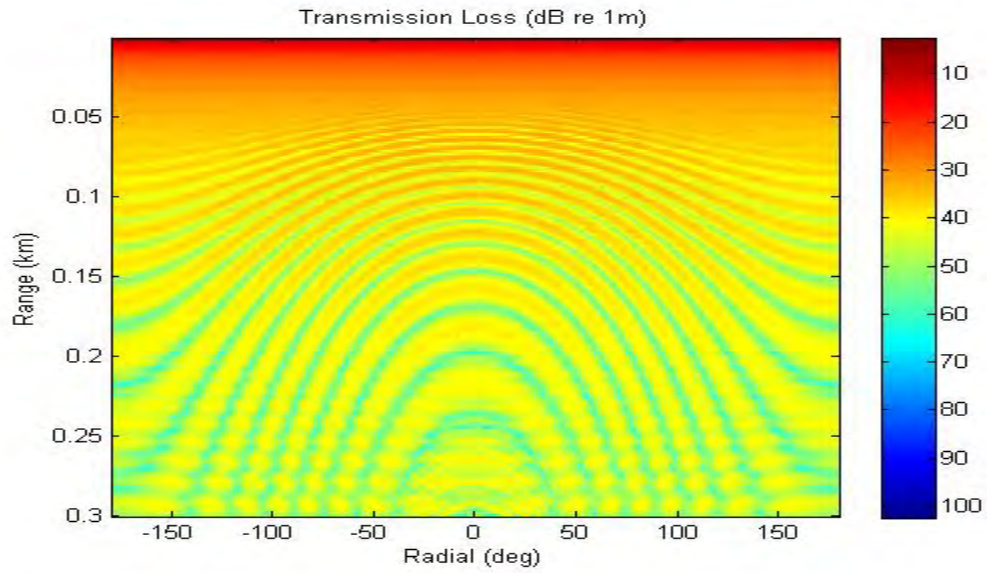


Figure 8. Transmission loss pattern at source depth.

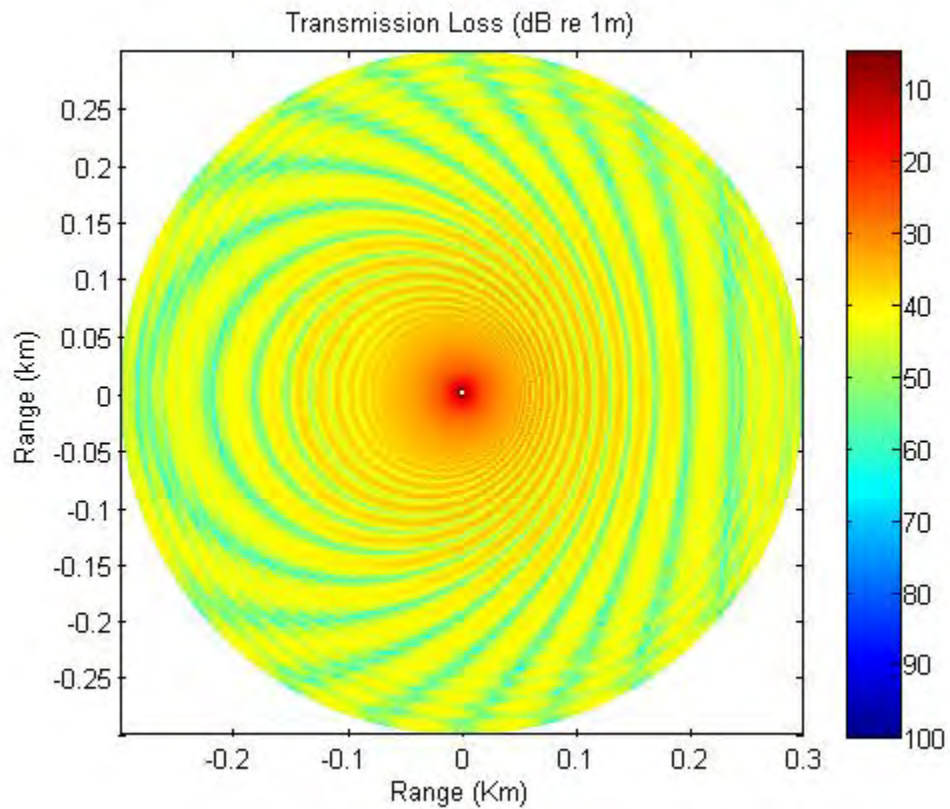


Figure 9. Constant slope surface effect on the waves emitted by a 50 m deep source.

2. Constant Slope Bottom and a Flat Surface

The corresponding solution is now computed by interchanging the surface and bottom characteristics. The environment now has a smooth flat surface with a sloped bottom which should produce the equivalent field solution, albeit rotated, as in the constant slope surface case. In this case, the surface depth is set to a constant value of zero and the source depth is shifted upwards to 30 m depth (consistent with source depth relative to the surface in the previous case), while the average depth of the medium will be 100 m. The 2-D bottom bathymetry for this environment is defined as

$$b_{dint} = b_{dint} - 0.1(r \cos \phi) \quad (65)$$

where “ b_{dint} ” is the interpolated bottom depth at each range step and ϕ is the bearing angle of propagation.

Figures 10 and 11 present the results along opposing radials. The results in these figures should compare directly, through a simple rotational transformation, to the results presented earlier in Figures 6 and 7.

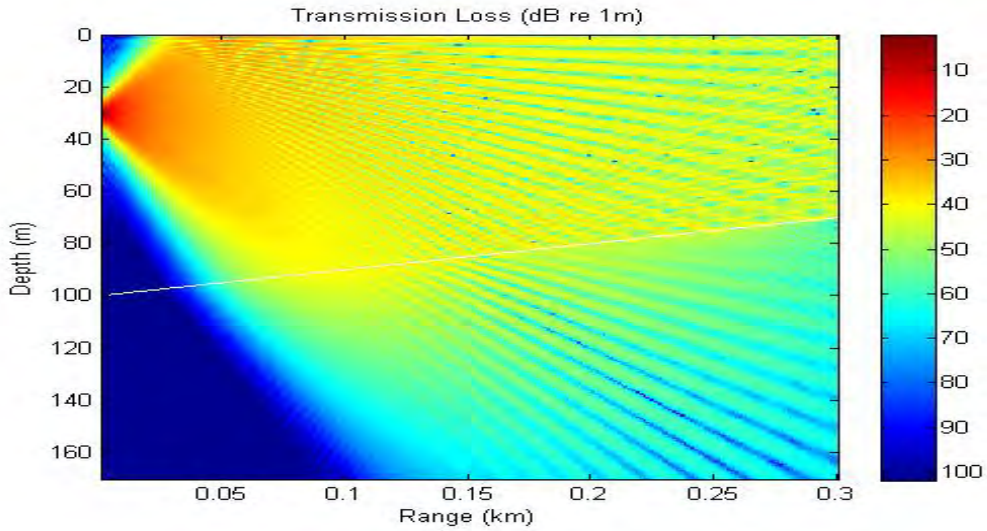


Figure 10. 0-degree radial for a source at depth of 30 m.

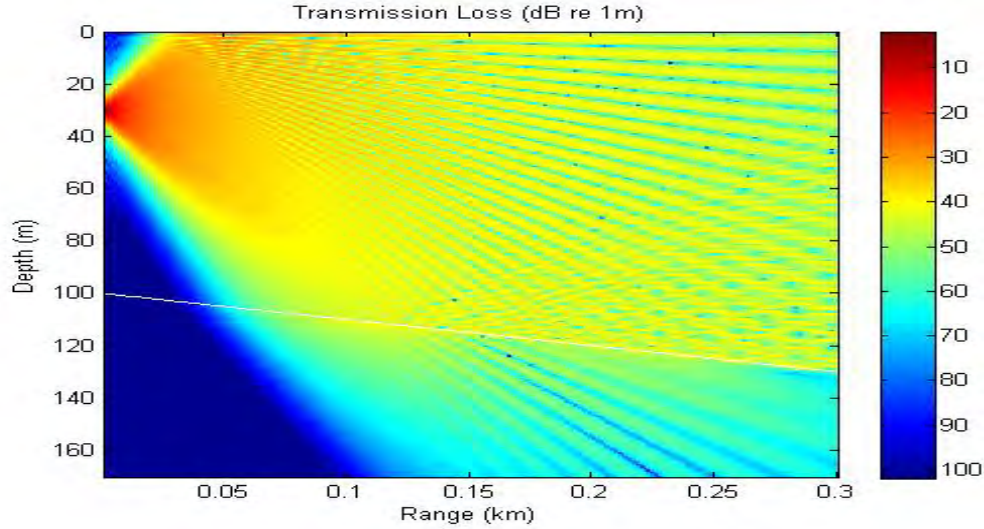


Figure 11. 180-degree radial for a source at depth of 30 m.

3. Constant Slope Surface Model versus Constant Slope Bottom Model

In order to compare results from the two different approaches, a common depth for extracting transmission loss must be defined. The most convenient depth to choose in both cases is the depth of the bottom bathymetry. Other than some geometrical rescaling (due to rotation) of the range from the source, the transmission loss traces along the bottom depth should agree between these two methods.

Figure 12 shows the initial results directly extracted from each solution at the bottom interface in polar coordinates. Due to the inclination presented by the sloping bottom model, we must adjust the range defined in the calculation in order to compare results. Figures 13 and 14 utilize this range-scaling correction to compare the transmission loss traces along opposing radials.

As can be noted in Figures 13 and 14, the comparison between solutions computed with a 2-D sloping bottom using the standard 3-D MMPE and this new algorithm with a 2-D sloping surface show good agreement.

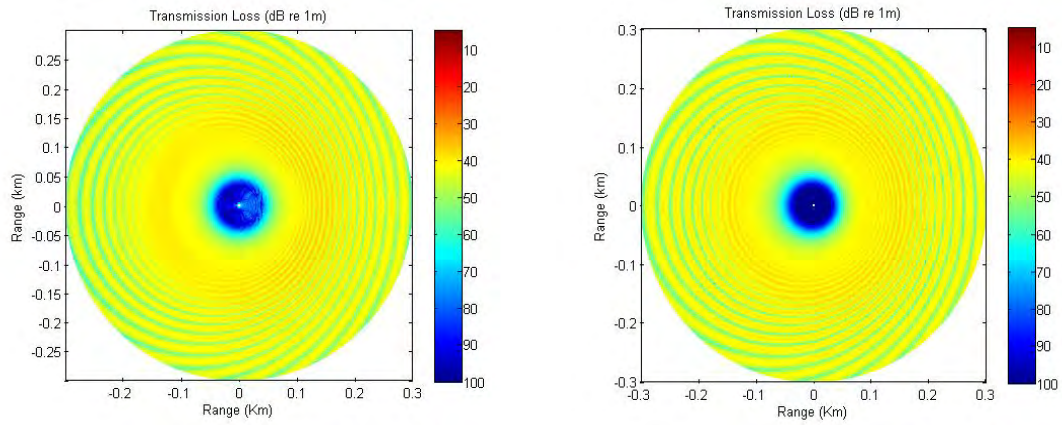


Figure 12. Model solutions for the water-bottom interface: (left) the constant slope surface; (right) the constant slope bottom.

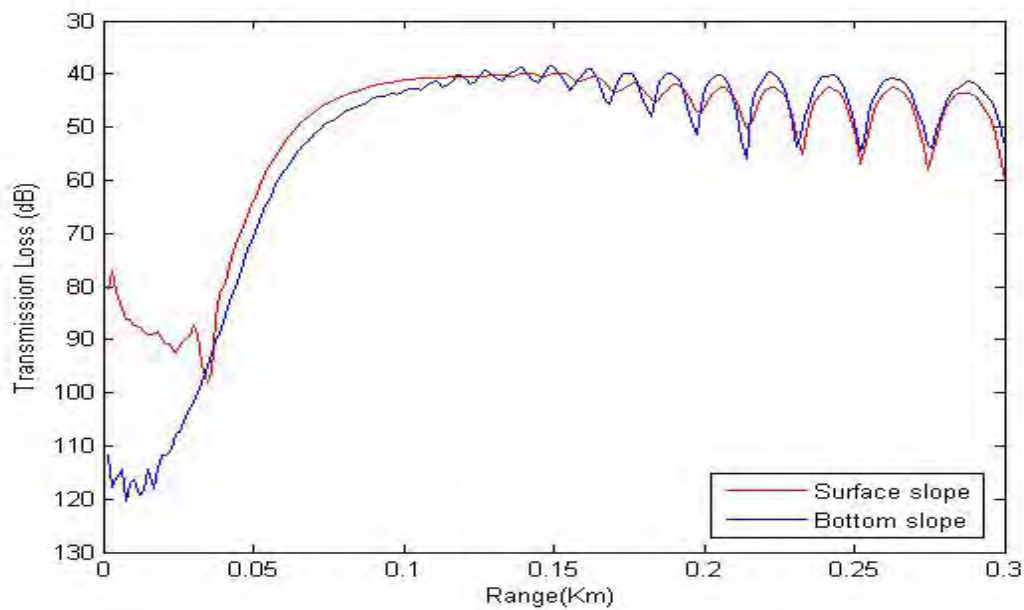


Figure 13. Transmission loss at water-bottom interface along the 0 radial.

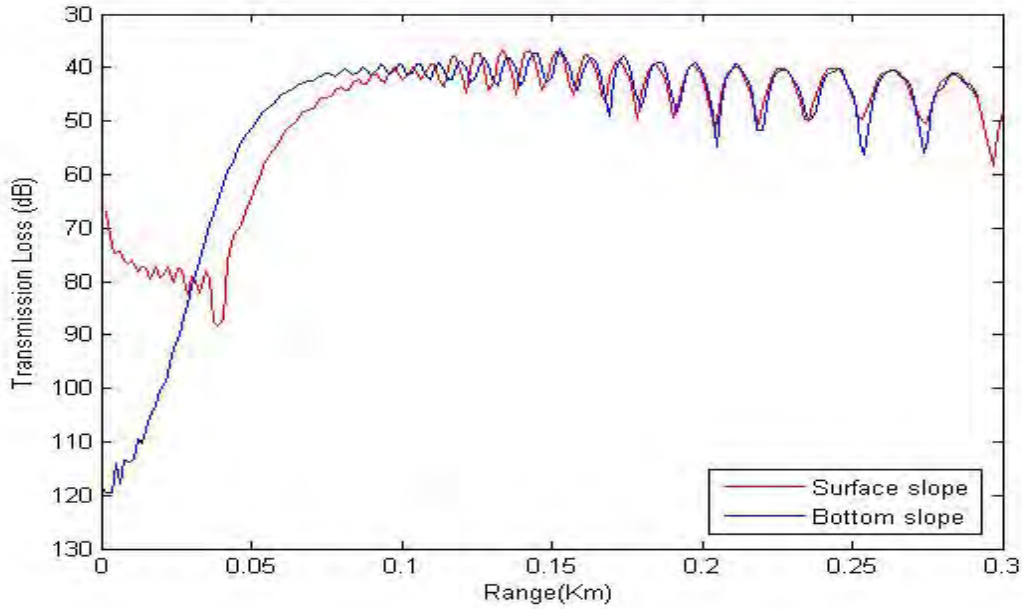


Figure 14. Transmission loss at water-bottom interface along the 180 radial.

B. CONCENTRIC SINUSOIDAL SURFACE PERTURBATIONS

As an alternative approach to confirm proper model behavior, we now examine the results derived from a surface perturbation defined as concentric sinusoidal waves. Theoretically, all the radials should be affected in the same manner due to the defined, radially-independent environment.

Figures 15 and 16 present the transmission loss field results from opposing radials. As expected, the results appear identical in their structure along each radial. Figure 17 displays the transmission loss results extracted from a constant depth of 30 m, the same as the source depth. The results transformed to polar coordinates are presented in Figure 18.

The results show, as expected, that the acoustic field will propagate identically along all bearing angles, producing the circular patterns shown in Figure 18.

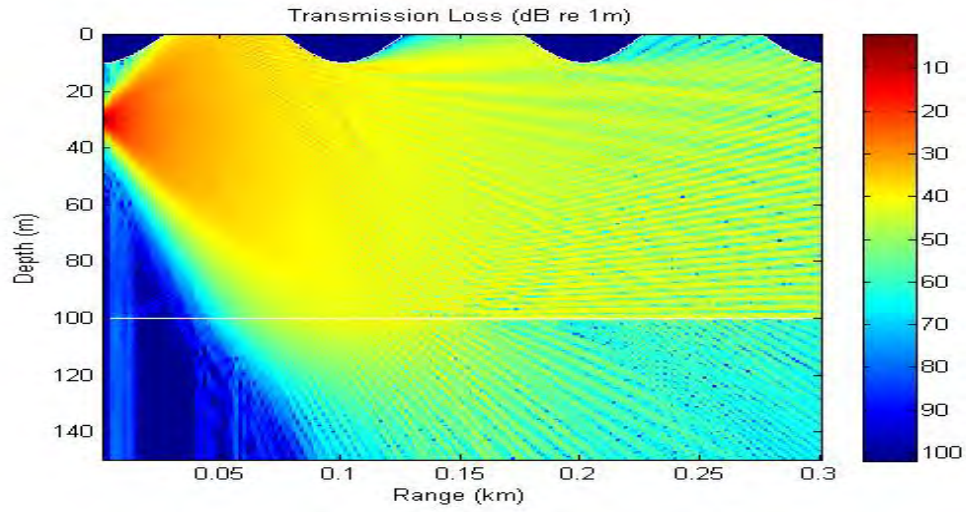


Figure 15. 0-degree radial for a source at depth of 30 m.

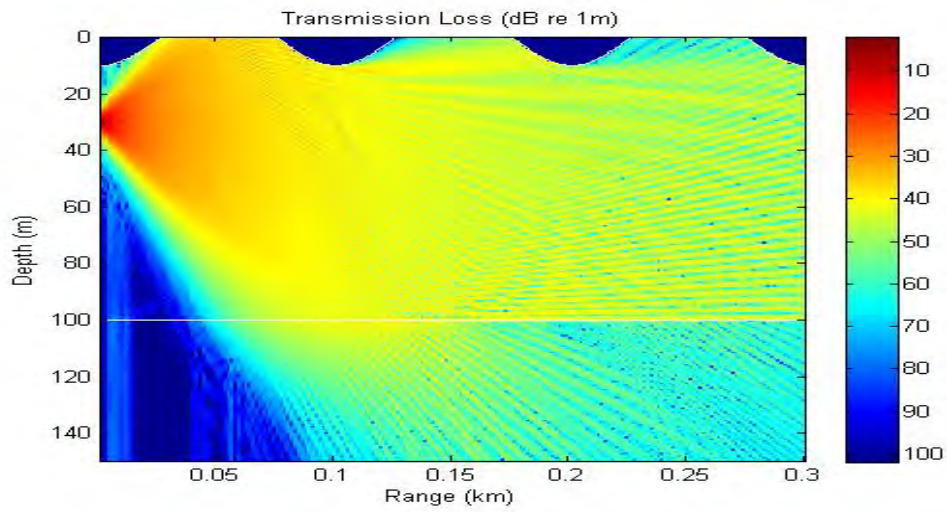


Figure 16. 180-degree radial for a source at depth of 30 m.

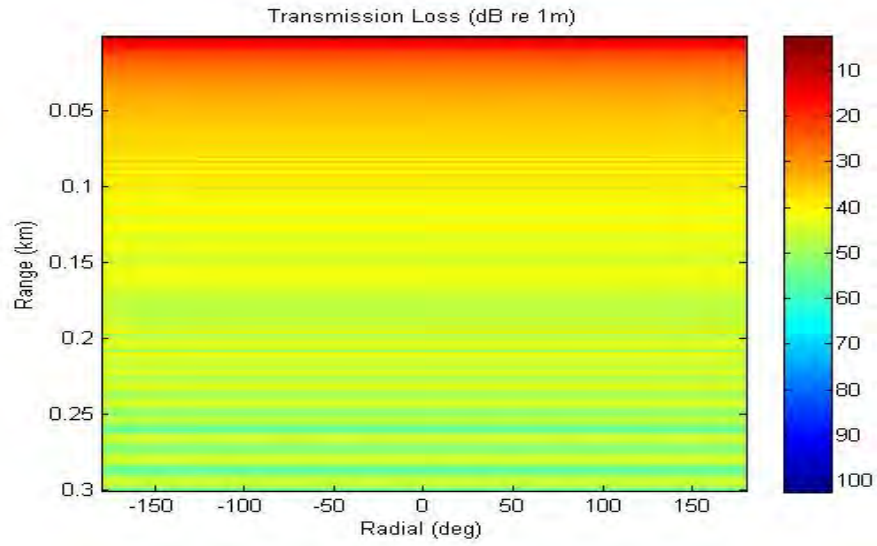


Figure 17. Transmission loss pattern at source depth.

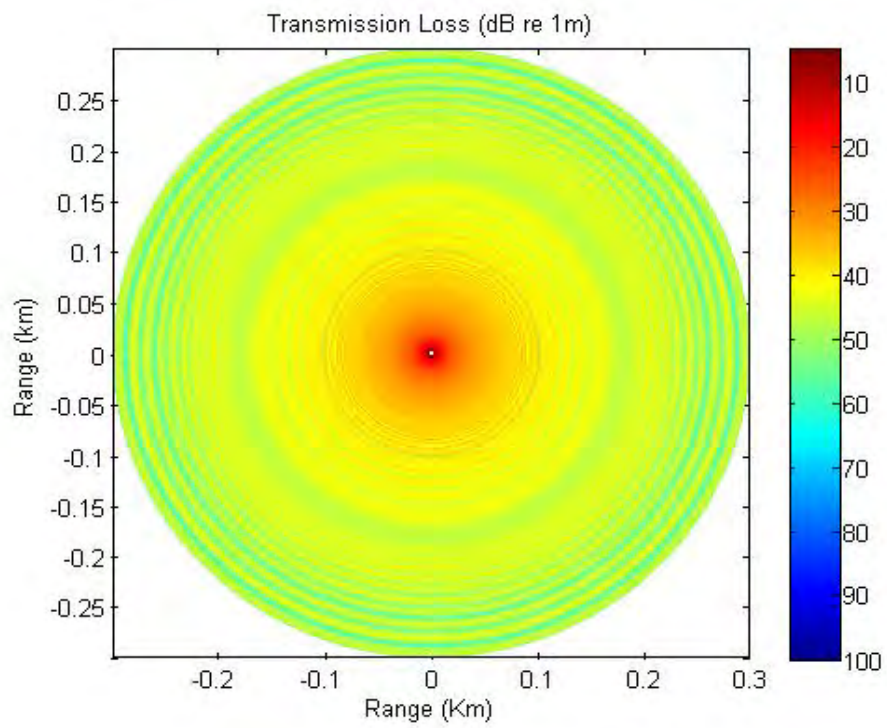


Figure 18. Concentric sinusoidal surface perturbations effect on a transmission loss field extracted at source depth.

C. PLANAR SINUSOIDAL SURFACE PERTURBATIONS

We now examine the results computing using the planar sinusoidal surface perturbations. While the forward and backward (0 and 180 degrees) radials should produce the same results due to symmetry, there should be significant differences between those and other radials, where the surface perturbation along the path is different.

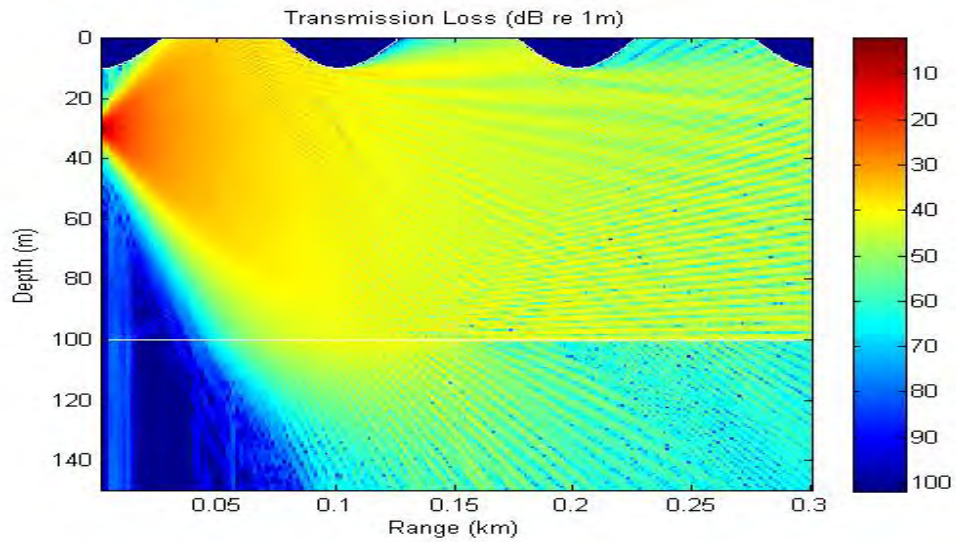


Figure 19. 0-degree radial for a source at depth of 30 m.

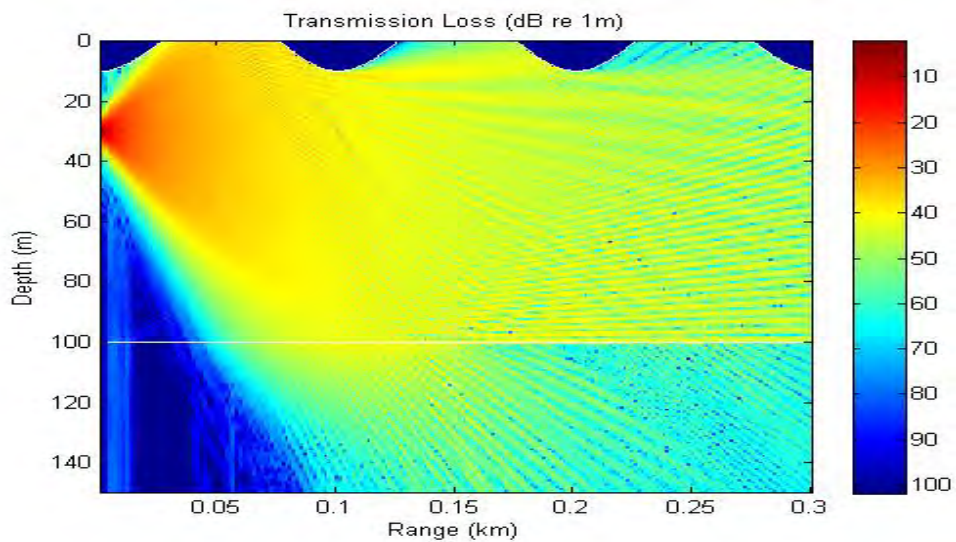


Figure 20. 180-degree radial for a source at depth of 30 m.

Figures 19 and 20 display the symmetric radials along 0 and 180 degrees. As expected, the transmission loss patterns appear identical between the two bearings. However, since the propagation will respond differently along each radial, an examination of the field at a single depth produces the results displayed in Figures 21 and 22.

Note that the dominant scattering features present (most notably in Figure 22) occur upon the first interaction with the downward perturbation of the surface roughness. The impact on the field is clearly parallel to the plane of the surface perturbation, and for ranges shorter than ± 0.1 km on the horizontal cross-range axis, energy appears to be channeled between the downward portions of the surface roughness on either side.

Beyond ± 0.1 km on the horizontal cross-range axis, the impact of the surface roughness is less noticeable. This is due to the dominant scattering occurring within the first ± 0.1 km. Beyond this range, much of the surface interaction has been shadowed by the near field scattering.

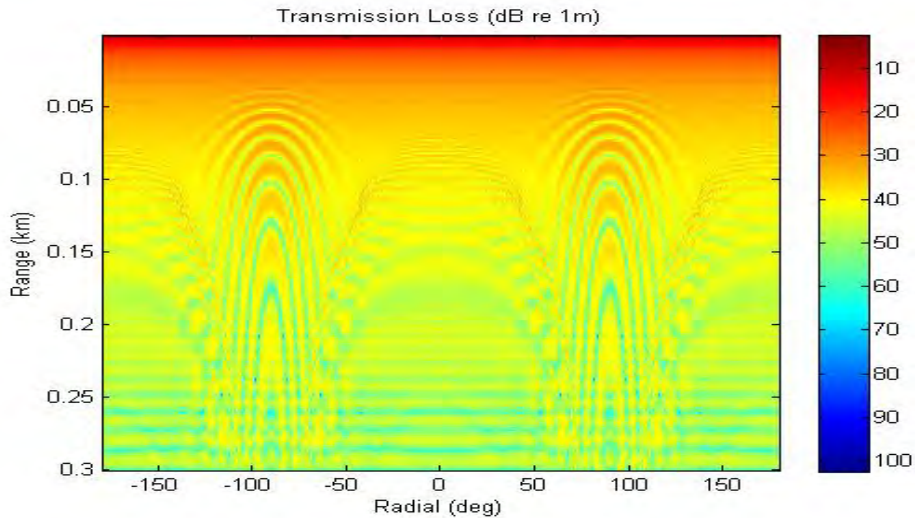


Figure 21. Transmission loss pattern at source depth.

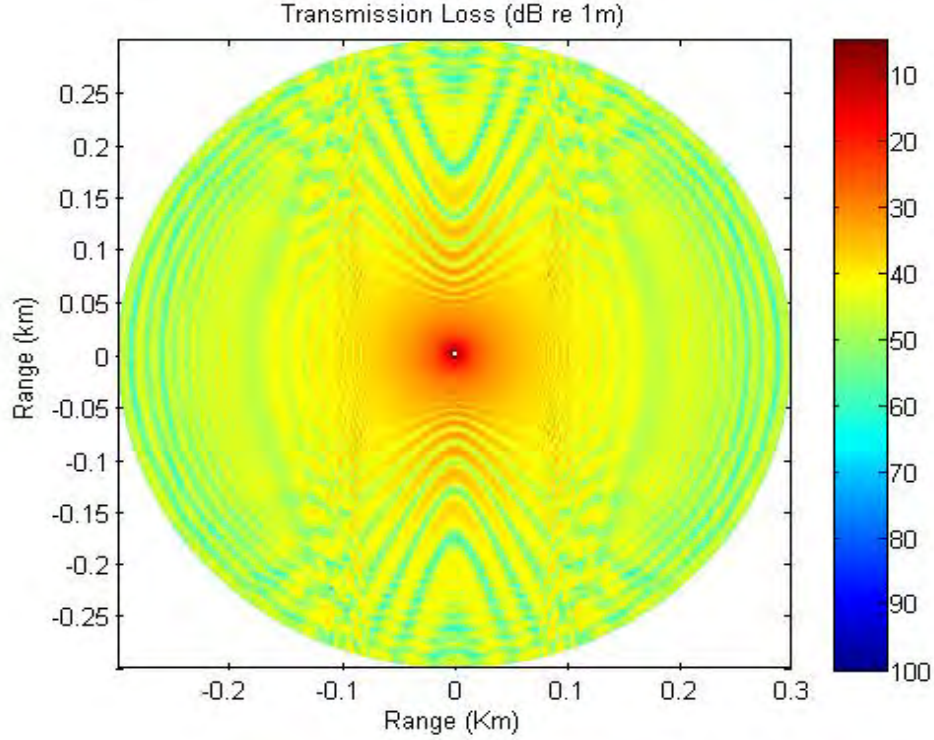


Figure 22. Planar sinusoidal surface perturbations effect on a transmission loss field extracted at source depth.

D. UPWARD SINUSOIDAL SURFACE PERTURBATIONS

In order to isolate some of the scattering phenomena occurring from the previous type of planar sinusoidal surface perturbation, and to break the symmetry of the problem to ensure proper model behavior, the next surface to test is simply a single sinusoidal surface displacement. We start initially by creating a single upward sinusoidal surface perturbation to the field, identical in form to the previous surface on one side only and out to 0.1 km. We select the 0 radial to represent the source front-side of the acoustic propagation and the 180 radial to show the response on the back-side of the source.

The results are presented in Figures 23 through 26. As expected, the back-side of the propagation shows little impact from the surface perturbation on the front-side. There may be some minor effect along the boundary separating front-side and back-side, but this is to be expected due to horizontal scattering. In addition, the scattering in the front-side direction is very similar to the previous multiple sinusoidal planar perturbation,

confirming that most of the scattering effects are due to the initial interactions with the downward sloping portion of the surface.

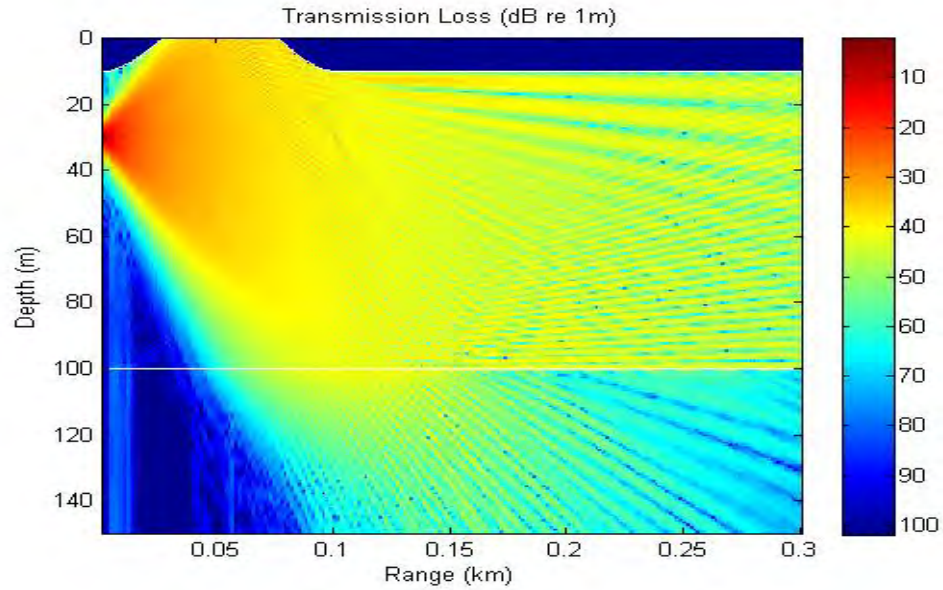


Figure 23. 0-degree radial for a source at depth of 30 m.

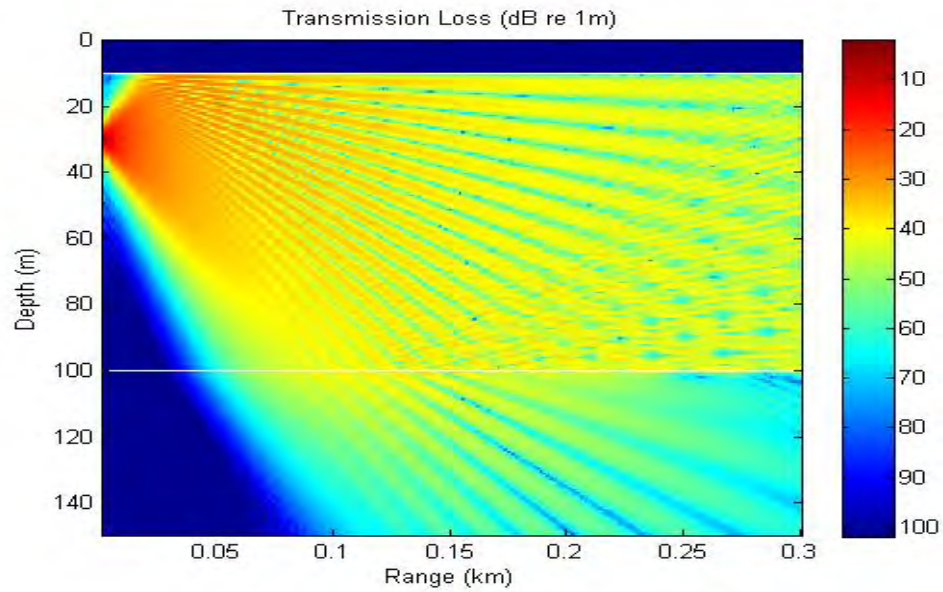


Figure 24. 180-degree radial for a source at depth of 30 m.

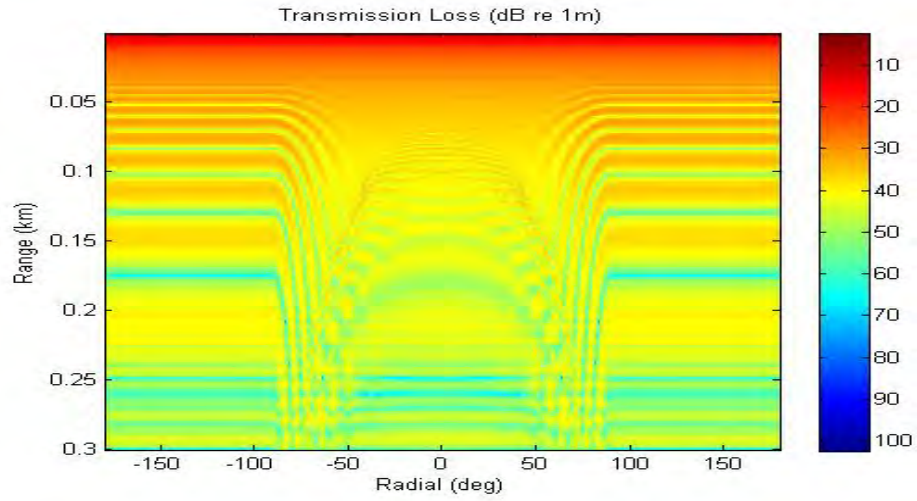


Figure 25. Transmission loss pattern at source depth of 30 m.

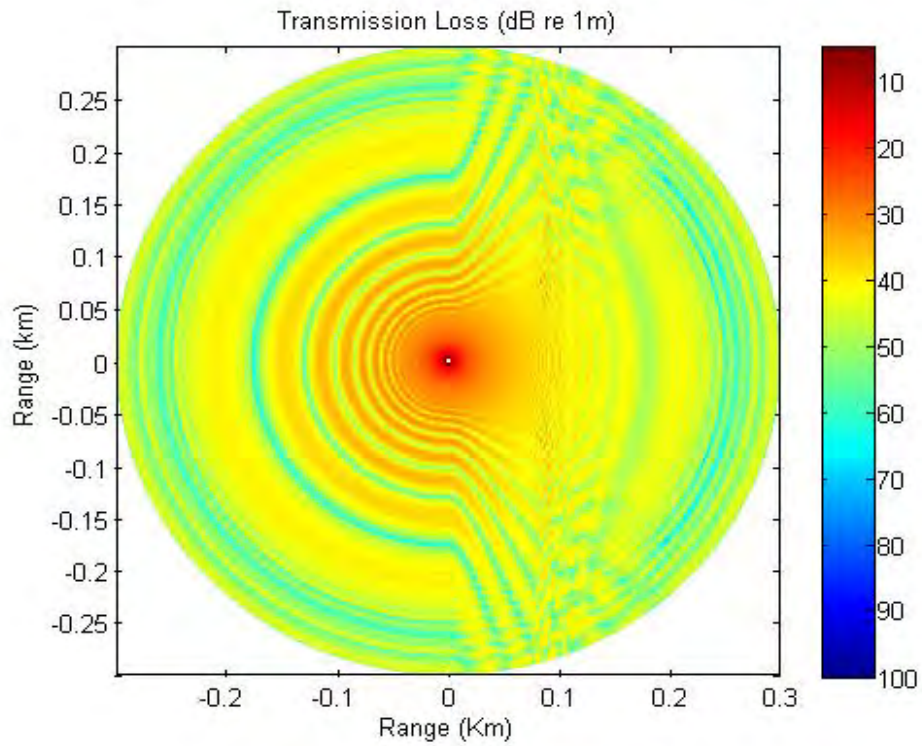


Figure 26. Upward sinusoidal surface perturbations effect on a transmission loss field extracted at source depth.

E. DOWNWARD SINUSOIDAL SURFACE PERTURBATIONS

As an alternative to the single sinusoidal planar perturbation presented previously, we also created a similar surface that perturbs the surface downward initially before returning upward to a constant depth. One of the primary differences of this perturbation was that it places the strongly scattering downward slope of the surface perturbation immediately adjacent to the source range. This would, therefore, be expected to introduce stronger scattering at higher angles, particularly in the near-field. As before, we choose the 0 radial to represent the front-side path of the acoustic propagation and the 180 radial to represent the back-side field of the source.

It is worth noting that during early testing of the model's stability, this particular surface perturbation initially generated non-physical results. Closer inspection revealed that the earlier version of the model was utilizing an SPE approximation to compute the azimuthal wavenumber propagator function, resulting in large scattering angles being misrepresented in the solution. As discussed in the theory section of this thesis, it is quite important to employ wide-angle approximations, even in cross-range/bearing-angle, in order to properly compute the azimuthal field structure. After upgrading the code to account for this, the results from this perturbation model became physically realizable. (All results reported in this thesis, therefore, utilized the WAPE approximation for all operators.)

Figures 27 through 30 display the computed transmission loss field results for this surface perturbation. Again, the back-side of the field shows little impact from the perturbation, except very near the edge separating the front-side from the back-side, which is to be expected. In addition, the front-side scattering is much stronger in this case than in the previous one. There is also clearly diffraction of the field filling in the classical shadow zone on the back-side of the downward surface perturbation.

It is natural to expect that the scattering from the front-side would eventually be transferred across the boundary to the back-side of the field. Because of the limitation on the source angle in the vertical, and the relatively short range of the calculations, this was

not clearly observed in any of these calculations. It is worth exploring this issue further in future analysis.

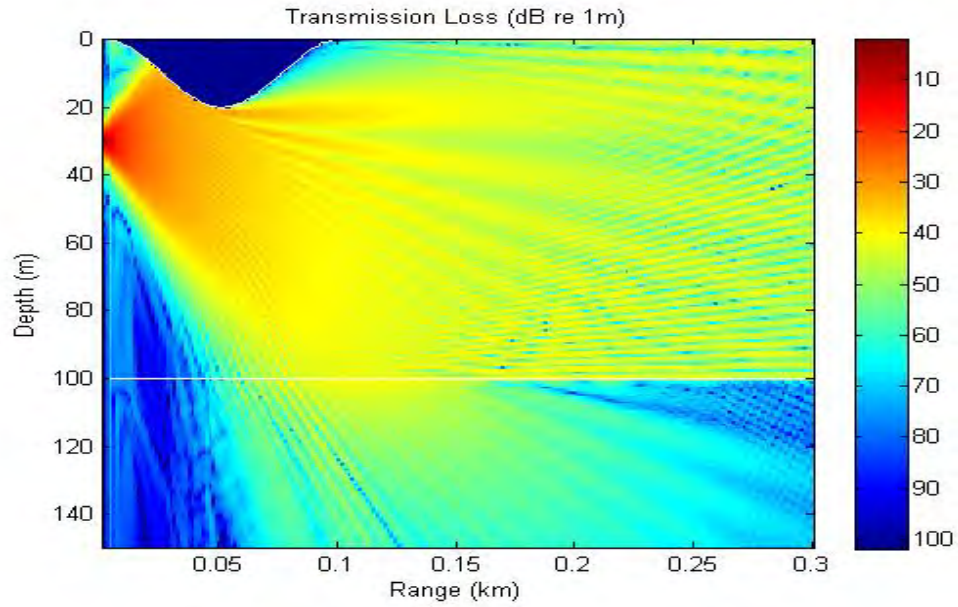


Figure 27. 0-degree radial for a source at depth of 30 m.

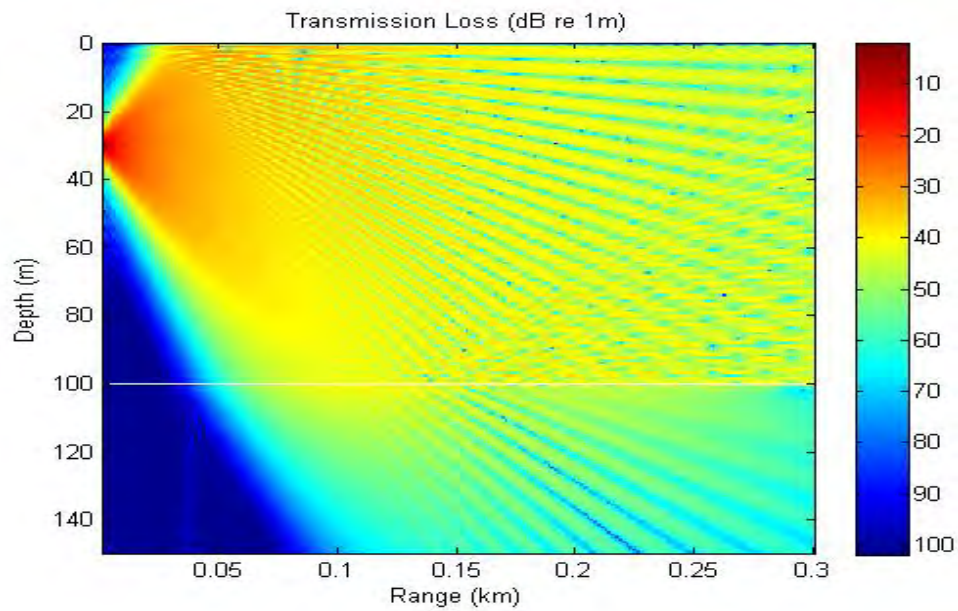


Figure 28. 180-degree radial for a source at depth of 30 m.

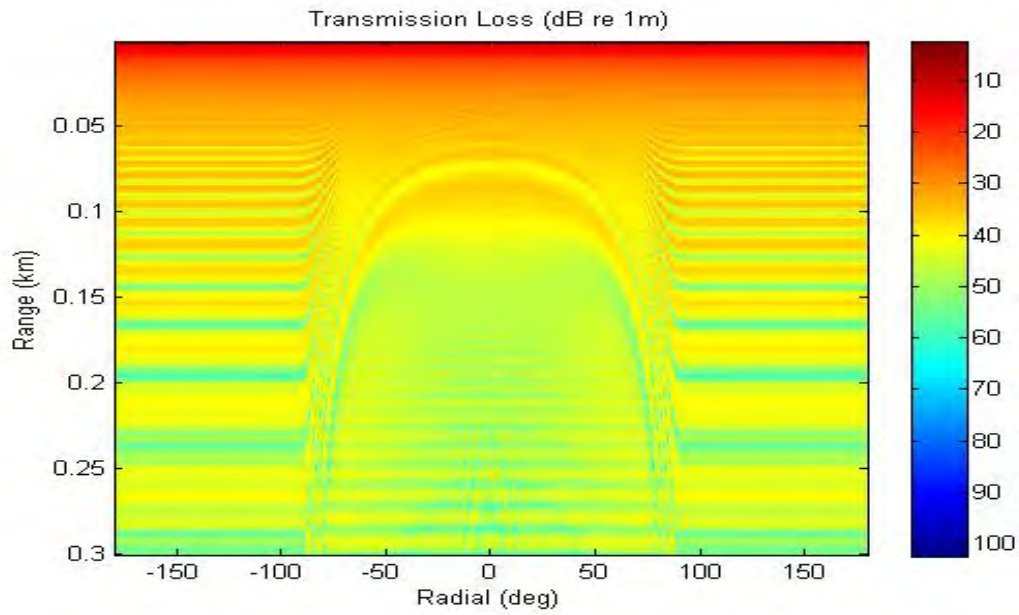


Figure 29. Transmission loss pattern at source depth.

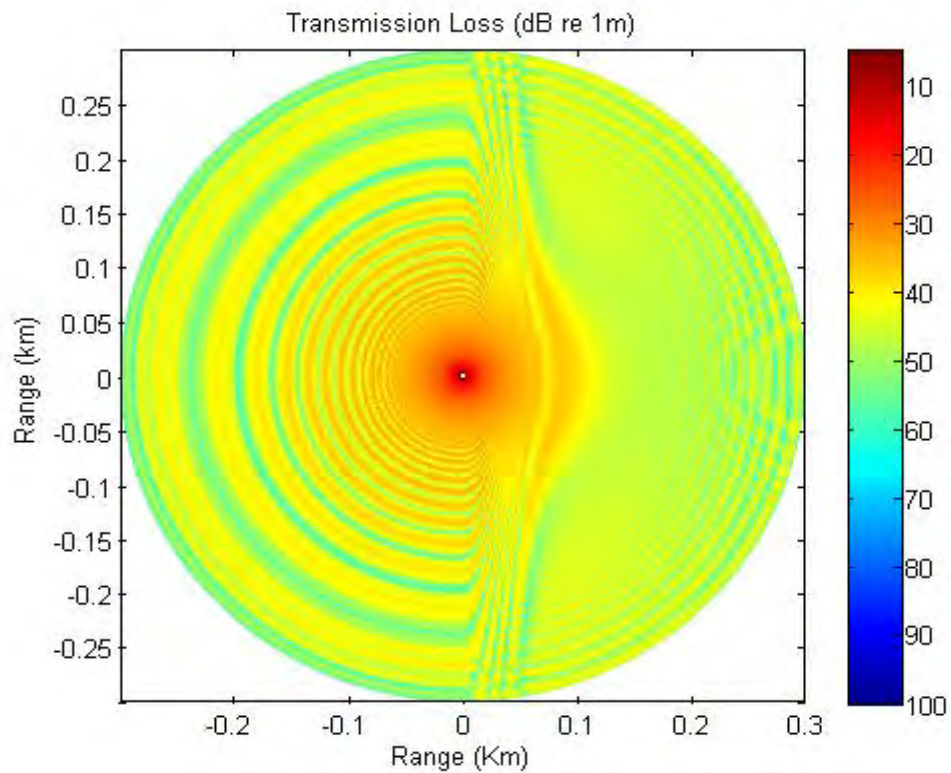


Figure 30. Downward sinusoidal surface perturbations effect on a transmission loss field extracted at source depth.

F. COMPARISON OF THE EFFECT OF 3-D VERSUS $N \times 2$ -D

One of the goals of this project is to develop an accurate means of computing the 3-D scattering from a rough 2-D surface, and then comparing solutions between this 3-D model and standard $N \times 2$ -D models. Such $N \times 2$ -D models are significantly more efficient and require much less in the way of computing power. And so, understanding when a true 3-D solution is required will help avoid unnecessary computational complexity. In this section, we will compare results computed between an $N \times 2$ -D version of the MMPE model that utilizes a consistent rough surface scattering algorithm with the 3-D version described in this thesis.

1. Constant Slope Surface Perturbations

Utilizing the same environment defined previously for the constant sloping surface, the results from the 3-D model and the corresponding $N \times 2$ -D version were computed out to a maximum range of 0.6 km. The goal of carrying out these calculations to a slightly longer range than before is simply to allow for more azimuthal coupling to occur which would differentiate the impact of the 3-D calculation. Figures 31 through 34 present the model results from this environment along the different radials and at a constant depth.

The results from the two models, particularly as displayed in Figure 34 in polar coordinates, show little difference between the models. This is perhaps not too surprising, since azimuthal coupling is known to have a larger impact at longer ranges. More significant differences would likely be observed if the calculations were carried out at a lower frequency and the maximum range was increased significantly. However, due to the nature of the sloping surface, longer ranges would cause the surface to cross the bottom interface, generating nonsensical environments.

In an effort to highlight the differences computed from the 3-D and $N \times 2$ -D models, Figure 35 displays the difference in transmission loss values at a constant depth. As noted previously, the differences are relatively minor, and only begin to become prominent at longer ranges. Furthermore, the strongest differences occur along the radials at 90 and 270 degrees, corresponding to bearings of constant surface depth. These

bearings also correspond to the maximum cross-range slopes of the surface, where we would expect to see the strongest amount of azimuthal coupling.

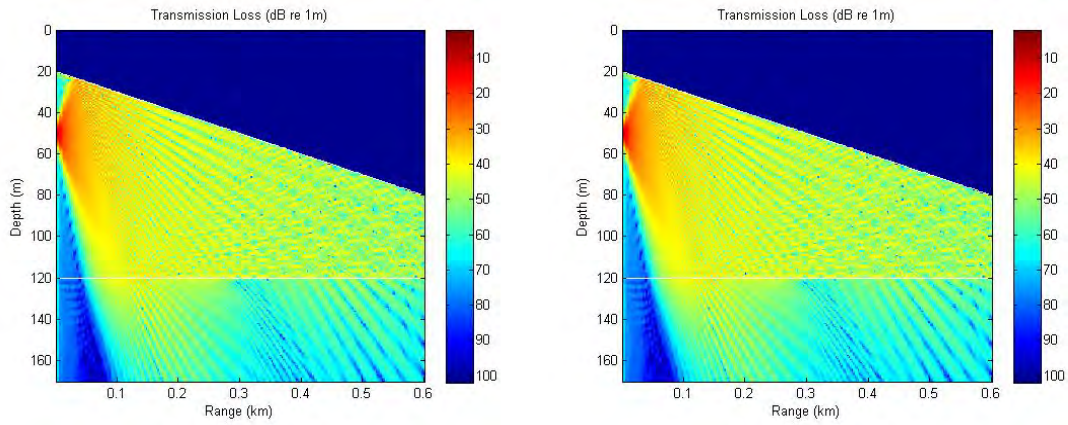


Figure 31. Model solutions for the constant slope surface perturbations along the 0 radial: (left) using the basic 2D interface perturbations model; (right) using the 3D model.

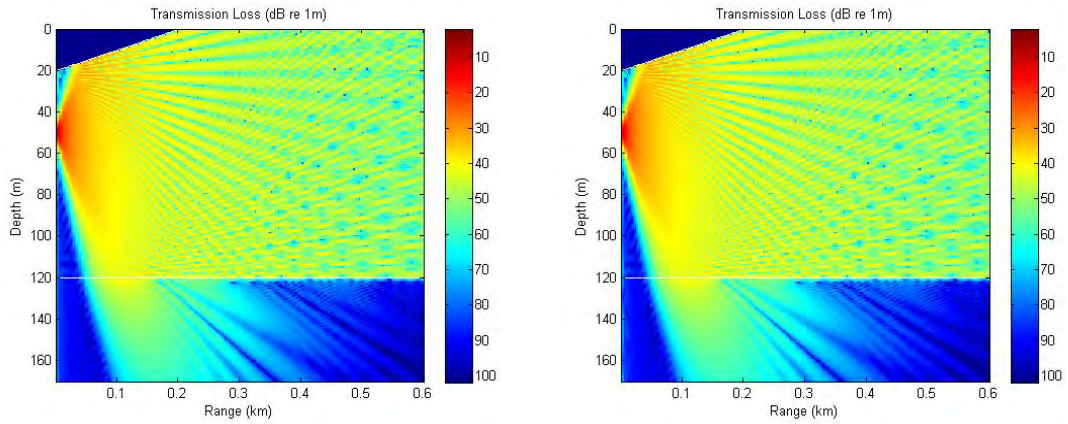


Figure 32. Model solutions for the constant slope surface perturbations along the 180 radial: (left) using the basic 2D interface perturbations model; (right) using the 3D model.

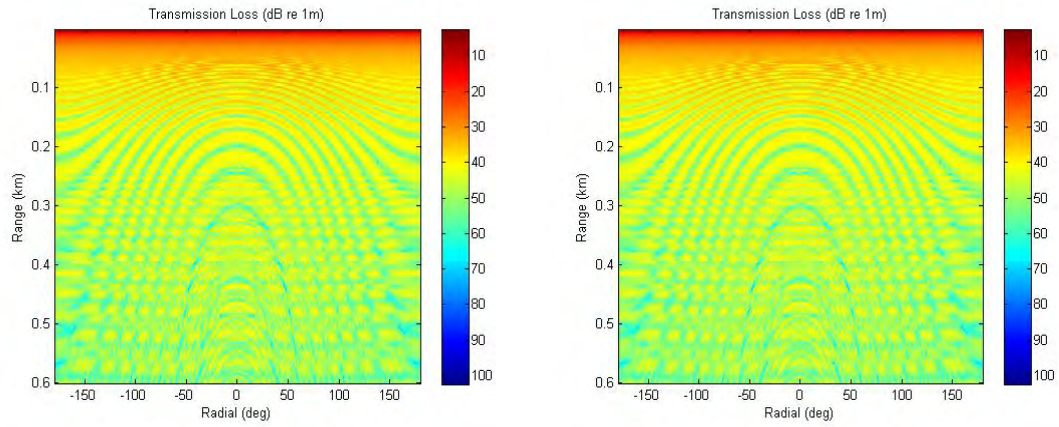


Figure 33. The wave pattern results for a 50 m deep source: (left) using the basic 2D interface perturbations model; (right) using the 3D model.

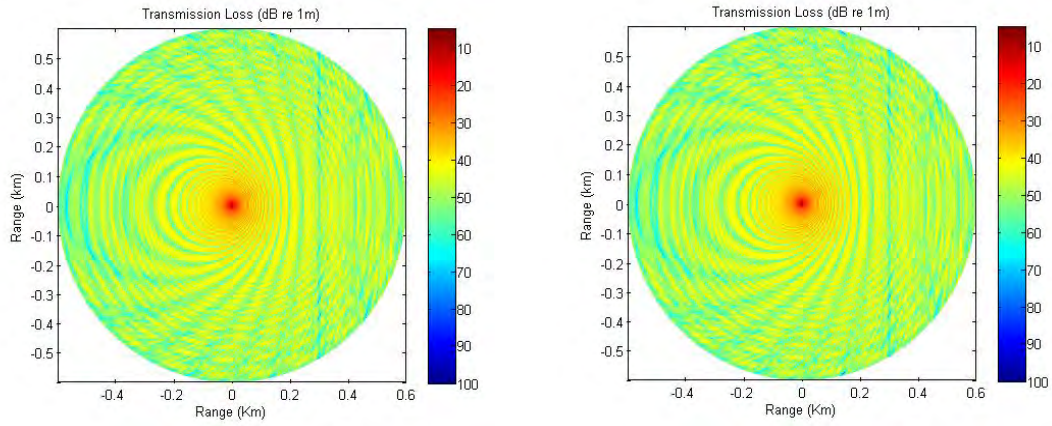


Figure 34. Model solutions for the constant slope surface perturbations effect on a 50 m deep source waves: (left) using the basic 2D interface perturbations model; (right) using the 3D model.

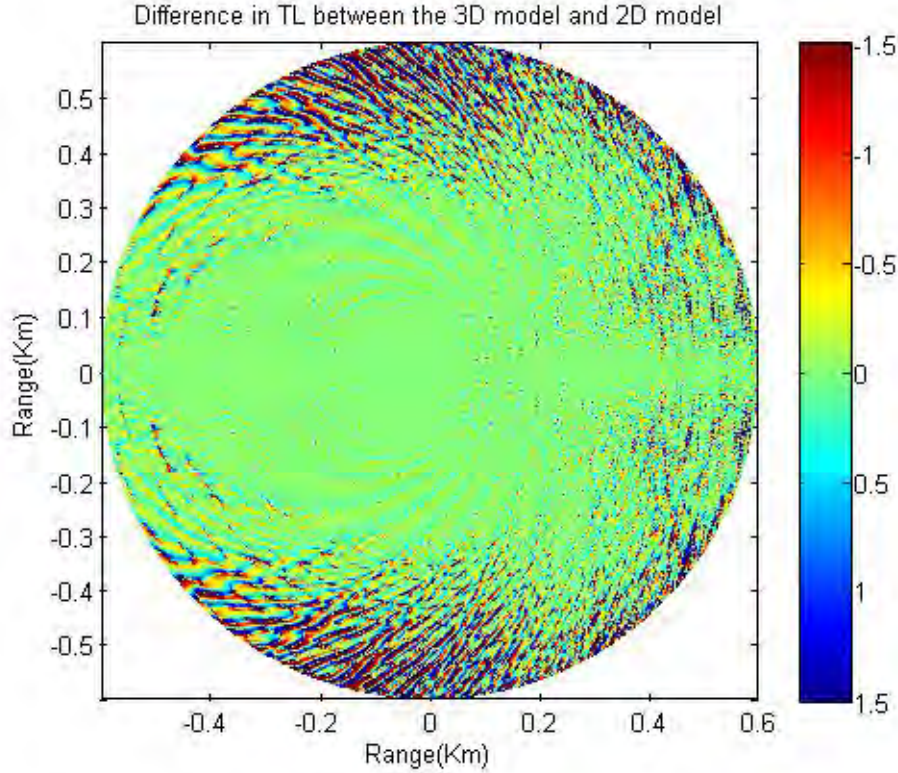


Figure 35. Difference in transmission loss values at a constant depth.

2. Downward Sinusoidal Surface Perturbations

The second environment we will consider for comparison between the fully 3-D results versus the Nx2-D approach corresponds to the single, downward sinusoidal surface perturbation. This perturbation produced the strongest scattering in the near-field, and would be expected to produce strong differences between 3-D and Nx-2D in the near-field, as well.

Figures 36 through 39 present the results from the two approaches for this environment. It is worth noting that the single radial results presented in Figure 36 show some marked differences in the field computed in the bottom when the full 3-D model is employed. This is due to high vertical angle scattering produced by the computational algorithm. The transmission loss levels of these differences are very low, however, nearly 120 dB below the primary energy observed in the water column, and are not of any physical significance.

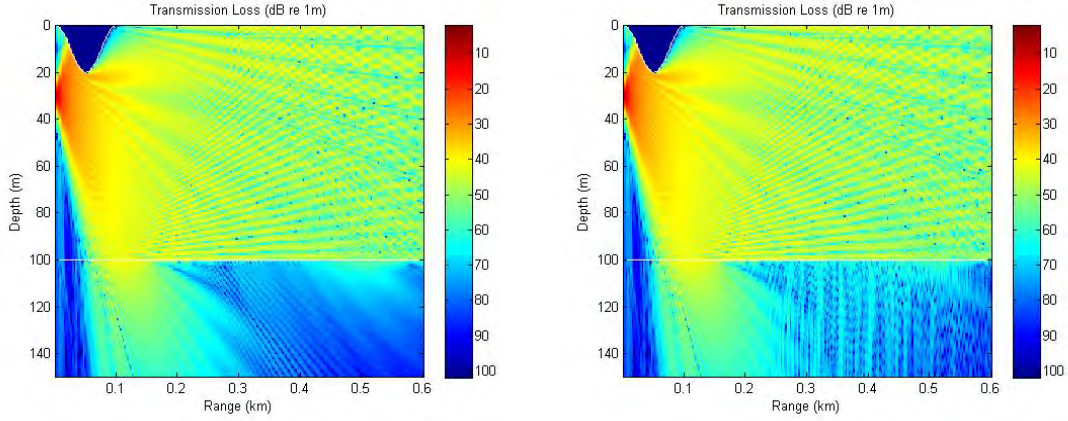


Figure 36. Model solutions for the downward sinusoidal surface perturbations along the 0 radial: (left) using the basic 2D interface perturbations model; (right) using the 3D model.

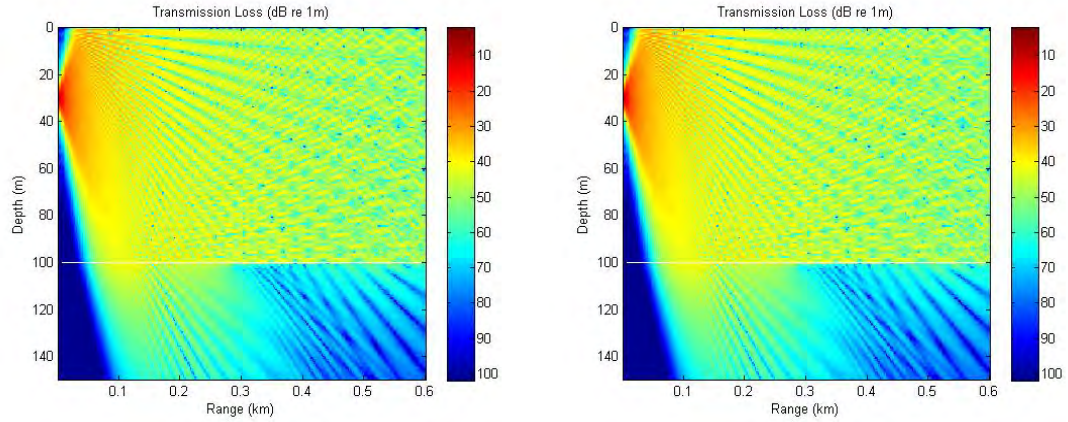


Figure 37. Model solutions for the downward sinusoidal surface perturbations along the 180 radial: (left) using the basic 2D interface perturbations model; (right) using the 3D model.

As before, the polar plots of the transmission loss field at a constant depth of 30 m displayed in Figure 39 shows little apparent difference in the solutions. In an effort to highlight the differences, Figure 40 shows the difference in transmission loss at a constant depth in polar coordinates. As before, the differences are observed to expand in range, and are strongest in regions where the cross-range slope of the surface perturbation is largest.

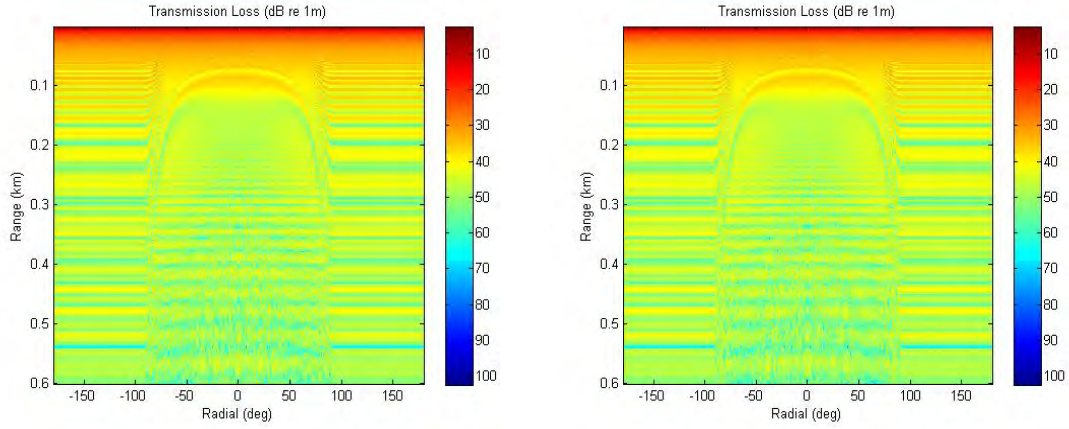


Figure 38. The wave pattern results for a 30 m deep source: (left) using the basic 2D interface perturbations model; (right) using the 3D model.

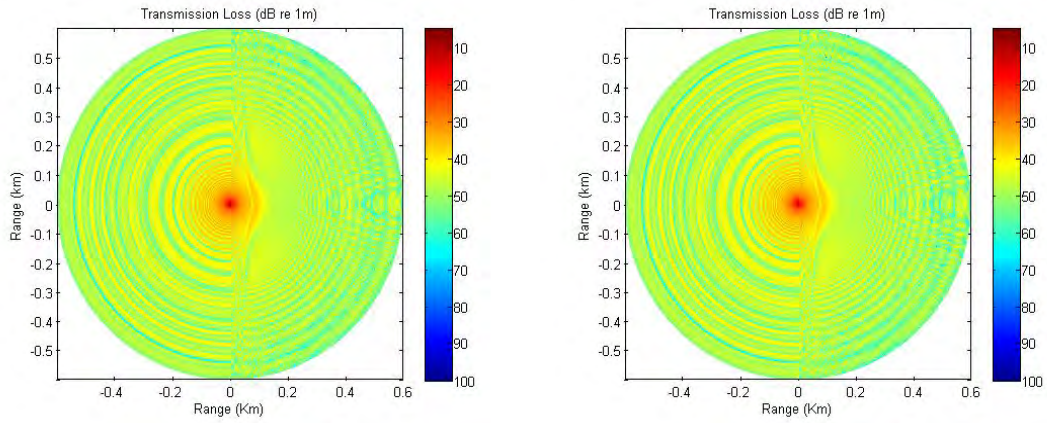


Figure 39. Model solutions for the downward sinusoidal surface perturbations on a 30 m depth source waves: (left) using the basic 2D interface perturbations model; (right) using the 3D model.

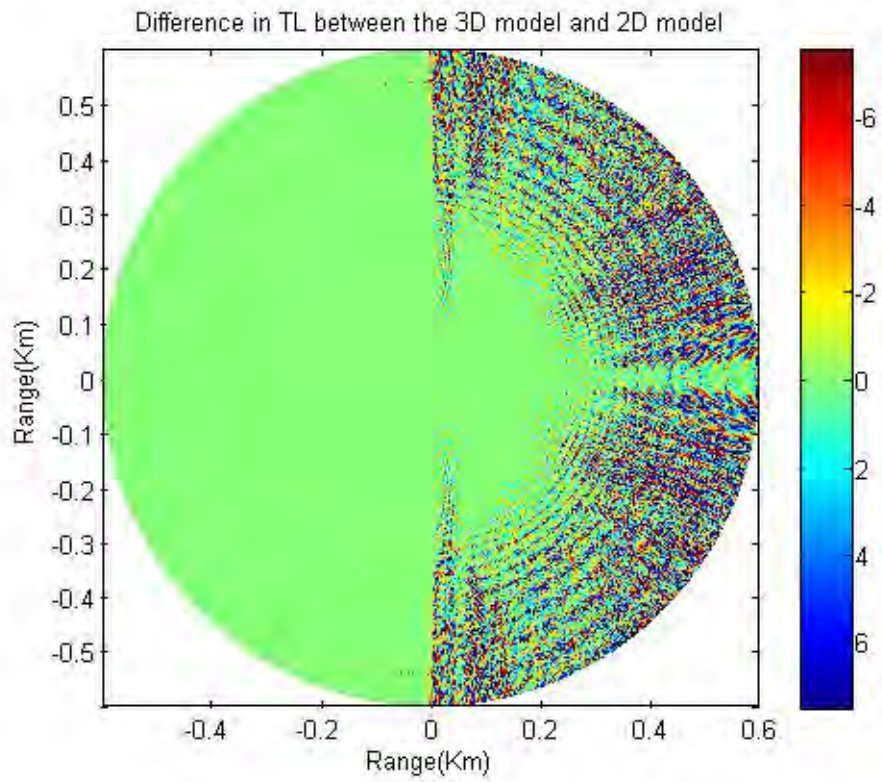


Figure 40. Difference in transmission loss values at a constant depth.

V. CONCLUSIONS AND FUTURE WORK

Rough surface scattering is an important mechanism for introducing signal variability into underwater acoustic systems such as acoustic communications. The significance of three-dimensional scattering effects from two-dimensional rough surfaces has been investigated by other researchers. However, whether the full 3-D calculations constitute a significant improvement to the simpler, Nx2-D calculations remains unclear. The goal of this thesis was then to upgrade an existing 2-D parabolic equation model to incorporate full 3-D surface scattering. This will allow future studies that can more directly compute the specific influence of 3-D, out-of-plane scattering from 2-D rough surfaces.

There were two primary advances made in this work towards the stated goal. First, a hybrid implementation for the parabolic equation model was formulated and incorporated into a version of the Monterey-Miami Parabolic Equation model. This hybrid method consisted of the standard split-step Fourier algorithm traditionally employed in MMPE, and also a finite difference method utilizing a Padé approximation for the cross-range operator associated with the cross-range scattering of the rough surface. The solution to the finite difference system of equations was accomplished through a standard tri-diagonal solver.

The second advance related to the wavenumber propagator functions employed by the 3-D model in cylindrical coordinates. Previous work assumed the azimuthal coupling was small enough that a standard parabolic equation approximation was sufficient. However, with some of the larger surface slopes investigated in this thesis, it was determined that a wide angle parabolic equation approximation was necessary in order to properly account for the cross-range scattering. Once this upgraded propagator was incorporated, the model results became physically realistic for all of the rough surfaces investigated.

Five different “rough” surfaces were defined for model testing. These were all simple, non-flat boundaries that increased in complexity. The first example studied was

simply a smooth, sloped surface. The resulting field appeared consistent with expectations. In order to validate these results, the model was recast to compute the solution for a flat surface with a sloping bottom. Through an environmental rotation, these results should be identical. A comparison of the model results confirmed that the sloping surface results produced valid solutions.

The second surface was defined by concentric, sinusoidal surface displacements. Being independent of bearing angle, this surface was designed to test the model calculations and ensure that no erroneous out-of-plane scattering was occurring when none was expected. The model results were consistent with this expectation.

The third, fourth, and fifth surface fluctuations were defined in terms of horizontally planar sinusoidal surface perturbations of varying types. While there was no formal solution to compare with the model results, the general behavior was consistent with expectations, where scattering was observed parallel to the surface wavefront.

Finally, model results for two of the surface perturbations were computed using both the 3-D version developed here, as well as the Nx2-D version previously developed. A comparison of the results showed the dominant differences along the directions with the greatest cross-range surface slopes, as expected.

Future work could entail longer range solutions in order to search for more obvious cross-range coupling. Using sources defined by individual waveguide modes could also be employed to more clearly delineate horizontal refraction. In addition, the model results examined in this thesis were computed using only a single frequency. Future work could examine broadband signals, and thereby compute pulse propagation travel times, which could also provide specific evidence of horizontal refraction and out-of-plane scattering.

LIST OF REFERENCES

- Biot, M. A. "Reflection on a Rough Surface from an Acoustic Point Source." *The Journal of the Acoustical Society of America* 29, no. 11 (April 1957): 1193–1200.
- Chimenti, D. E., and O. I. Lobkis. *Effect of Rough Surface on Guided Waves in Plates*. Ames, IA: Plenum Press, 1998.
- Collins, M. D. "Benchmark Calculations for Higher-Order Parabolic Equations." *Journal of the Acoustical Society of America* 87 (1990): 1535–1538.
- Dahl, P. H. "High Frequency Forward Scattering from the Sea Surface: The Characteristic Scales of Time and Angle Spreading." *IEEE Journal Of Ocean Engineering* 26 (2001): 141–151.
- Gilbert, Freeman, and Leon Knopoff. "Seismic Scattering from Topographic Irregularities." *Journal of Geophysical Research* 65, no. 10 (1960): 3437–3444.
- Holfford, R L. "Scattering of Sound Waves at a Periodic, Pressure-release Surface: An Exact Solution." *The Journal of the Acoustical Society of America* 70 (Oct 1981): 1116–1128.
- Karjadi, Entin A., Mohsen Badiy, James T. Kirby, and Cihan Bayindir. "The Effects of Surface Gravity Waves on High-Frequency Acoustic Propagation in Shallow Water." *Journal of Oceanic Engineering*, September 2011: 1–10.
- Liu, Jin Yuan, Chen Fen Huang, and Ping Chang Hsueh. "Acoustic Plane Wave Scattering from a Rough Surface Over a Random Fluid Medium." *Ocean Engineering* (National Sun Yat-sen University) 29 (May 2001): 915–930.
- Medwin, H., and C. S. Clay. *Fundamentals of Acoustical Oceanography*. Waltham, MA: Academic Press, 1998.
- Ogilvy, J A. "Wave Scattering from Rough Surfaces." Vers. 50. *IOP Science*. Theoretical Physics Division, Harwell Laboratory. July 6, 1987. Accessed October 10, 2013. <http://iopscience.iop.org/>
- Ostashev, V. E., D. Juve, and P. Blanc-Benon. "Derivation of a Wide-Angle Parabolic Equation for Sound Waves in Inhomogeneous Moving Media." *ACUSTICA*, 1997: 455–460.
- Press, W. H., S. A. Teukolsky, W. T. Vetterling, and B. P. Flannery. *Numerical Recipes: The Art of Scientific Computing*. 3rd ed. New York: Cambridge University Press, 2007.

- Senne, Joseph. "Modeling of Acoustic Propagation for High Frequency Transmissions under Variable Sea Surfaces." Ph.D. dissertation, University of Delaware, 2012.
- Shchegrov, A. V. "Propagation of Surface Acoustic Waves Across the Randomly Rough Surface of an Anisotropic Elastic Medium." *Journal Of Applied Physics*. April 12, 1995. Accessed October 10, 2013. <http://dx.doi.org/10.1063/1.360250>
- Smith, K. B., and F. D. Tappert. *UMPE: The University of Miami Parabolic Equation Model, Version 1.0*. Memo, Marine Physical Laboratory Tech., 1993.
- Smith, K., and J. Colosi. "Effects of Solitons on Acoustic Energy Flow in Three Dimensions." *Journal of Acoustical Society of America* 123 (2008): 3942.
- Smith, Kevin B. "Convergence, Stability, and Variability of Shallow Water Acoustic Predictions using, a Split-Step Fourier Parabolic Equation Model." *Journal of Computational Acoustics* 9 (2001): 243–285.
- . "Field Transformational Approach to Three-Dimensional Scattering from Two-Dimensional Rough Surfaces." *Journal of Acoustical Society of America* 131 (2012): 441–447.
- Tappert, F. D. "The Parabolic Approximation Method," in *Lecture Notes in Physics: Wave Propagation and Underwater Acoustics* (pp. 224–287). Vol. 70. Edited by J. B. Keller and J. S. Papadakis. New York: Springer-Verlag, 1977.
- Thomson, D. J., and N. R. Chapman. "A Wide-Angle Split-Step Algorithm for the Parabolic Equation." *Journal of Acoustical Society of America* 74 (1983): 1848–1854.
- Thorsos, Eric I, and Shira Lynn Broschat. "An Investigation of the Small Slope Approximation for Scattering from Rough Surfaces. Part I. Theory" *The Journal of the Acoustical Society of America* 97, no. 4 (April 1995): 2082–2093.
- Thorsos, Eric I, and Shira Lynn Broschat. "An Investigation of the Small Slope Approximation for Scattering from Rough Surfaces. Part II. Numerical Studies." *The Journal of the Acoustical Society of America* 101, no. 5 (May 1997): 2615–2625.
- Williams, Kevin L., Eric I. Thorsos, and W. T. Elam. "Examination of Coherent Surface Reflection Coefficient (CSRC) Approximations in Shallow Water Propagation." *The Journal of the Acoustical Society of America* 116, no. 4 (October 2004): 1974–1984.
- Yevick, D., and D. J. Thomson. "A Hybrid Split-Step/Finite-Difference PE Algorithm for Variable-Density Media." *Journal of Acoustical Society of America* 101 (1997): 1328–1335.

INITIAL DISTRIBUTION LIST

1. Defense Technical Information Center
Ft. Belvoir, Virginia
2. Dudley Knox Library
Naval Postgraduate School
Monterey, California